HHS Public Access

Author manuscript

Cell Metab. Author manuscript; available in PMC 2024 July 02.

Published in final edited form as:

Cell Metab. 2024 April 02; 36(4): 762–777.e9. doi:10.1016/j.cmet.2024.01.006.

PHLDA2-mediated phosphatidic acid peroxidation triggers a distinct ferroptotic response during tumor suppression

Xin Yang[1], **Zhe Wang**[1], **Sviatlana N. Samovich**[2,3], **Alexander A. Kapralov**[2], **Andrew A. Amoscato**[2], **Vladimir A. Tyurin**[2], **Haider H. Dar**[2], **Zhiming Li**[1], **Shoufu Duan**[1], **Ning Kon**[1], **Delin Chen**[1], **Benjamin Tycko**[4], **Zhiguo Zhang**[1,5], **Xuejun Jiang**[6], **Hülya Bayir**[2,3,7], **Brent R. Stockwell**[8,9], **Valerian E. Kagan**[2], **Wei Gu**[1,10,11,*]

[1]Institute for Cancer Genetics, and Herbert Irving Comprehensive Cancer Center, Vagelos College of Physicians & Surgeons, Columbia University, New York, NY 10032, USA.

[2]Center for Free Radical and Antioxidant Health and Departments of Environmental Health, Chemistry, Pharmacology and Chemical Biology, Radiation Oncology, University of Pittsburgh 15261, PA, USA.

[3]Department of Pediatrics, Division of Critical Care and Hospital Medicine, Redox Health Center, Vagelos College of Physicians and Surgeons, Columbia University Irving Medical Center, New York, NY 10032, USA.

[4]Hackensack Meridian Health Center for Discovery and Innovation, Nutley, NJ 07110, USA.

[5]Department of Pediatrics, and Department of Genetics and Development, Vagelos College of Physicians & Surgeons, Columbia University, New York, NY 10032, USA.

[6]Cell Biology Program, Memorial Sloan-Kettering Cancer Center, New York, NY 10065, USA.

[7]Department of Critical Care Medicine, Safar Center for Resuscitation Research, University of Pittsburgh, Pittsburgh, PA 15224, USA.

[8]Department of Chemistry, Columbia University, New York, NY 10027, USA.

[9]Department of Biological Sciences, Columbia University, New York, NY 10027, USA.

[10]Department of Pathology and Cell Biology, Vagelos College of Physicians & Surgeons, Columbia University, New York, NY 10032, USA.

[11]Lead Contact

Summary

[*]Correspondence to Wei Gu (wg8@cumc.columbia.edu).

Contributions

Conception and experimental design: X.Y., B.H., V.E.K., and W.G. LC-MS analysis: S.N.S., A.A.K., A.A.A., V.A.T., and H.H.D. CRISPR Screen: X.Y., Z.W., Z.L., S.D., and Z.Z. Cell experiments: X.Y., Z.W., and D.C. Animal experiments: X.Y., and N.K. Manuscript writing: X.Y., B. T., X.J., H. B., B.R.S., V.E.K., and W.G.

Declaration of interests

B.R.S. is an inventor on patents and patent applications involving small molecule drug discovery and ferroptosis; holds equity in Sonata Therapeutics, holds equity in and serves as a consultant to Exarta Therapeutics and ProJenX, Inc. and serves as a consultant to Weatherwax Biotechnologies Corporation and Akin Gump Strauss Hauer & Feld LLP. X.J. is an inventor on patents related to autophagy and cell death; and holds equity of and consults for Exarta Therapeutics and Lime Therapeutics. The other authors declare no competing interests.

Although the role of ferroptosis in killing tumor cells is, well established, recent studies indicate that ferroptosis inducers also sabotage the anti-tumor immunity by killing neutrophils thus unexpectedly, stimulate tumor growth, raising a serious issue about whether ferroptosis effectively suppresses tumor development *in vivo*. Through genome-wide CRISPR-Cas9 screenings, we discover a PHLDA2-mediated ferroptosis response that is neither ACSL4-dependent nor requires common ferroptosis inducers. PHLDA2-mediated ferroptosis acts through peroxidation of phosphatidic acid (PA) upon high levels of ROS. ROS-induced ferroptosis is critical for tumor growth in the absence of common ferroptosis inducers; strikingly, loss of PHLDA2 abrogates ROS-induced ferroptosis and promotes tumor growth but has no obvious effect in normal tissues in both immunodeficient and immunocompetent mouse tumor models. These data demonstrate that PHLDA2-mediated phosphatidic acid peroxidation triggers a distinct ferroptosis response critical for tumor suppression and reveal, that PHLDA2-mediated ferroptosis occurs naturally *in vivo* without any treatment from ferroptosis inducers.

Keywords

PHLDA2; cystine starvation; ROS; ferroptosis; cancer; tumor suppression; GPAT3; p53; ALOX12; phosphatidylethanolamine; phosphatidic acid; lipid peroxidation

Introduction

Ferroptosis is an iron-dependent form of cell death that occurs when excess levels of oxygenated lipids disrupt the integrity of cellular membranes[1, 2]. Dissection of the roles and mechanisms of ferroptosis reveals new insights into tumor suppression and tumor immunity, which provides new therapeutic strategies for treating cancers by targeting the vulnerability of cancer cells[3]. Ferroptosis has been shown to be a natural defense against cancer development[4, 5]. For example, p53 tumor suppressor represses solute carrier family 7 member 11 (SLC7A11) expression to restrain the uptake of cystine and sensitize cancer cells to ferroptosis for tumor suppression[6, 7], whereas a p53 hotspot mutation p53-R175H displays gain-of-function activities to promote tumor growth by abrogating ferroptosis induced by BTB and CNC homology 1 (BACH1)[8]. Indeed, several additional metabolic targets of p53 also contribute to its ferroptotic response, and the defects in p53-mediated ferroptosis caused by an African-specific polymorphism in the TP53 gene impair its tumor suppressor function[9–12]. Moreover, BRCA1-associated protein 1 (BAP1), another well-known tumor suppressor that encodes a nuclear deubiquitinating enzyme, represses SLC7A11 expression and promotes ferroptosis by modulating histone H2A ubiquitination[13] and activation of ferroptosis becomes a valuable tool to targeting the vulnerability of human cancer cells[14]. Conversely, nuclear factor erythroid 2-related factor 2 (NRF2), a master antioxidant regulator, plays a major role in protecting the tumor cells from ferroptosis by upregulating SLC7A11, ferroptosis suppressor protein 1 (FSP1), and other cellular factors against ferroptosis induction[15–19]. In contrast, repression of NRF2 function by the tumor suppressor proteins such as Kelch-like ECH-associated protein 1 (KEAP1) and ARF promotes ferroptosis[20]. The dynamic regulation of ferroptosis is also implicated by the Retinoblastoma (RB)-E2F axis[21, 22], and the complexity of ferroptosis in tumor suppression is also observed[23]. Recent studies showed that the oncogenic PI3K-PTEN-mTORC axis

is involved in ferroptosis resistance through modulating glutathione peroxidase 4 (GPX4) expression and fatty acid metabolism[24, 25]. Nevertheless, context-dependent regulation of ferroptosis and additional ferroptosis pathways independent of the GPX4/ ACSL4 (long-chain-fatty-acid-CoA ligase 4) pathway are implicated under different physiological settings[26, 27].

Interestingly, several studies showed that ferroptosis is critical in T cell immunity and cancer immunotherapy[28]. $CD8^+$ cytotoxic T cells, the major executors of anti-tumor immunity in the tumor microenvironment, secrete interferon-γ (IFNγ) to promote ferroptosis in tumors[29–31]. Mechanistically, IFNγ released from $CD8^+$ T cells is able to suppress cystine uptake in tumor cells by downregulating SLC7A11 to trigger ferroptotic responses. Surprisingly, one recent study reported that ferroptosis in pathologically activated neutrophils induces the release of oxygenated lipids and limits the activity of T cells, which sabotages the anti-tumor immunity[32]. Kim et al. further showed that, in contrast to the tumor suppressive effects observed in the immunodeficient mouse model, the treatment of imidazole ketone erastin (IKE), a well-known ferroptosis inducer, enhances tumor formation in the immunocompetent mice[32]. Indeed, previous study indicated that ferroptotic cancer cells lack immunogenicity, which impedes antigen presentation and hinders therapeutic applications of ferroptosis[33]. Certain obstacle effects of ferroptotic cell death signals (e.g., prostaglandin E_2 and oxidized phospholipids) in immune response were also reported[34–37]. It is worth noting that despite the ferroptosis response induced by GPX4 inhibitors is ACSL4-dependent[38, 39], hepatocyte-specific inactivation of the *ACSL4* gene does not promote tumorigenesis *in vivo*; instead, suppresses tumor formation in the liver cancer tumor model[40]. Thus, although the complexity of ferroptosis in tumor development and its precise role in immunotherapy needs further investigation, it clearly raises an important issue of whether ferroptosis induction is effective for tumor suppression in the immunocompetent environment.

Here, through genome-wide CRISPR-Cas9 loss-of-function screenings, we discovered pleckstrin homology-like domain family A member 2 (PHLDA2), a phospholipid-binding protein, as a major factor in inducing ferroptosis in tumor cells. PHLDA2 is not required for the ferroptosis induced by GPX4 inhibitors but is essential for the ferroptosis induced by high levels of reactive oxygen species (ROS) or cystine starvation. The levels of ROS are much higher in cancer cells than in normal cells, which may make the cancer cells more susceptible to ROS-induced ferroptosis. Indeed, loss of PHLDA2 in tumor cells promotes tumor growth by abrogating ROS-induced ferroptosis without any obvious effect on cell proliferation or apoptosis. Moreover, we found that PHLDA2-mediated ferroptosis is required for tumor suppression in drug-induced liver cancer and *Eμ-Myc* induced lymphoma mouse models. Our study underscores a distinct ferroptotic response critical for tumor suppression in both immunodeficient and immunocompetent environments, occurring naturally *in vivo* without any treatment from ferroptosis inducers.

Results

Identification of PHLDA2 as a critical factor for ferroptosis induced by cystine starvation independent of GPX4 inhibition

Intracellular levels of the reduced glutathione (GSH) and ROS are highly dependent on the efficient import of cystine. It is believed that ferroptosis induced by cystine deprivation is critical for tumor cells under metabolic stress since nutrition deprivation is one of many types of metabolic stress during cancer development[41, 42]. To further elucidate the mechanism by which ferroptosis is regulated under metabolic stress, we performed a comparative CRISPR-Cas9 screening in human cancer cells upon ferroptosis induction either by cystine starvation or the treatment by RSL-3, a well-known GPX4 inhibitor (Figure S1A). To identify all the key factors required for ferroptosis, we used a genome-wide CRISPR-Cas9 knockout library that targets 18,436 genes with 5 single-guide RNAs (sgRNAs) per gene for the screening. Those cells that retained viability after ferroptosis triggering were collected and their sgRNAs were amplified, sequenced, and finally analyzed by using the Model-based Analysis of Genome-wide CRISPR-Cas9 Knockout (MAGeCK) method (Figures S1B and S1C)[43].

As the rate-limiting factor for GSH biosynthesis, the depletion of cystine is able to reduce intracellular GSH levels and subsequently suppress GPX4 activity. Thus, ferroptosis induced by cystine starvation is caused, at least in part, by GPX4 inhibition[26]. As expected, several but not all well-known factors that are involved in regulating ferroptosis induced by GPX4 inhibitors were also obtained in cystine starvation screening, including ACSL4 and lysophosphatidylcholine acyltransferase 3 (LPCAT3). Surprisingly, we identified PHLDA2 as a key factor for ferroptosis upon cystine starvation but not upon GPX4 inhibition (Figure S1C). PHLDA2 is a member of the PHLDA family, also known as TSSC3. PHLDA2 coded by an imprinting gene called *Ipl* (or *Tssc3*) on distal chromosome 7 of the mouse and human chromosome 11p15.5 is tightly regulated by DNA-methylation *in vivo*[44]. Notably, PHLDA2 is not required for normal development, and *Phlda2*-null mice display no obvious effects in their normal adult tissues[44], although its absence leads to placental overgrowth[45], and it has been found to be overexpressed in placentas associated with cases of human fetal growth restriction which is consistent with a cell context- dependent growth restraining role[46, 47]. Moreover, PHLDA2 exerts a tumor-suppressive function in several types of human cancers[48, 49]. Nevertheless, the precise role of PHLDA2 remains largely unclear.

To dissect how PHLDA2 promotes ferroptosis during cystine starvation, we generated PHLDA2-null, ACSL4-null, and PHLDA2/ACSL4-double-null A375 cells (Figure 1A). Both PHLDA2-null and ACSL4-null cells were partially resistant to cystine-starvation-induced ferroptosis. PHLDA2/ACSL4-double-null A375 cells displayed even greater resistance to ferroptosis (Figures 1B and S1D), while the levels of lipid peroxidation were also reduced more significantly in the double-null cells than in either PHLDA2-null or ACSL4-null cells under the same treatment (Figure 1C). Moreover, we also examined these cells in ferroptosis induced by RSL-3. As expected, loss of ACSL4 displayed complete resistance to ferroptosis, but no obvious effects were detected in PHLDA2-null cells (Figures

1D and 1E), suggesting that PHLDA2 and ACSL4 promote ferroptosis through different mechanisms.

Since cystine depletion in cells results in the upregulation of ROS levels, in addition to suppressing GPX4 function through depletion of GSH, we tested whether PHLDA2 is also involved in ferroptosis induced by high levels of ROS. To this end, we treated the cells with organic peroxides, tert-butyl hydroperoxide (TBH), or cumene hydroperoxide (CMH) to mimic the high levels of ROS conditions. By examining the effects of apoptosis, necroptosis, and ferroptosis inhibitors, we found that the short period of treatment of TBH- or CMH-triggered cell death was entirely ferroptosis (Figures 1F and 1G). Interestingly, in contrast to ferroptosis induced by RSL-3, loss of PHLDA2 but not ACSL4 was crucial for the resistance to ferroptosis induced by TBH or CMH (Figures 1H, 1I, and S1E). Further, the specific ferroptosis-promoting effects of PHLDA2 upon high levels of ROS were further validated in several different human cancer cell lines. As shown in Figures S1F–S1I, human lung adenocarcinoma A549 cells bearing knockouts of the ACSL4 or PHLDA2 genes were resistant to RSL-3 or TBH/CMH treatment, respectively. Moreover, knocking down PHLDA2 by small interfering RNA or knocking out PHLDA2 by sgRNAs rendered human osteosarcoma U2OS cells insensitive to ferroptosis upon high levels of ROS treatment (Figures 1J–1M and S1J–S1L). Ablation PHLDA2 expression in human breast cancer MCF7 cells also abrogated the ferroptosis response upon the same treatment (Figures 1N–1P) without any effect on other types of cell death such as apoptosis or necroptosis (Figure S1M). Consistently, overexpressed PHLDA2 promoted TBH-induced ferroptosis in A549, A375, and MCF7 cells (Figures 1Q–1T, S1N, and S1O), further validating a regulatory role of PHLDA2 in ferroptosis upon high levels of ROS.

Next, we generated GPX4-null, GPX4/ACSL4-double-null, and GPX4/PHLDA2-double-null cells (Figure S1P). As expected, GPX4-null cells underwent ferroptosis in the absence of ferroptosis inhibition. Indeed, loss of ACSL4 completely rescued the cell death induced by GPX4 inactivation, whereas loss of PHLDA2 showed no effect (Figure S1Q). Finally, we established GPX4/ACSL4/PHLDA2 triple knockout cells for further validation (Figure S1R). Again, although PHLDA2 was not required for the ferroptotic response induced by GPX4 inhibition (Figure S1S), loss of PHLDA2 rendered the GPX4/ACSL4 double null cells resistant to ROS-induced ferroptosis (Figure S1T). Together, these data indicate that PHLDA2 is required for ferroptosis induced by cystine starvation or high levels of ROS independent of the GPX4-ACSL4 axis.

PHLDA2 plays an important role in modulating ROS-induced ferroptosis by interacting the ALOX12 lipoxygenase

In our previous study, we identified 12-lipoxygenase (ALOX12), which catalyzes the oxygenation of polyunsaturated fatty acids (PUFA), as a critical factor for the ferroptosis response induced by high levels of ROS[7]. Thus, it is conceivable that PHLDA2 may regulate ROS-induced ferroptosis through the same pathway. To explore this possibility, we used a two-step affinity chromatography protocol (first with streptavidin agarose beads and then with S-protein agarose beads)[50, 51] to isolate ALOX12-associated proteome from human lung carcinoma H1299 cells that stably expressed SFB-ALOX12 protein

(Figure 2A). By analyzing the affinity-purified ALOX12-associated proteome by liquid chromatography-mass spectrometry/mass spectrometry (LC-MS/MS), we found two unique peptide sequences matching PHLDA2 (Figure 2A). We successfully verified the MS results by detecting PHLDA2 from the immunoprecipitated complexes of ALOX12 (Figure 2B)

To further validate the interaction between PHLDA2 and ALOX12 under physiological conditions, we performed the immunoprecipitation assay to examine the interaction between endogenous PHLDA2 and ALOX12 in U2OS cells. As shown in Figure 2C, endogenous ALOX12 was co-immunoprecipitated with endogenous PHLDA2 by an anti-PHLDA2 polyclonal antibody but not the anti-IgG control. Consistently, endogenous PHLDA2 was detected in the immunoprecipitated protein complex by an anti-ALOX12 monoclonal antibody (Figure 2D), validating that ALOX12 is a *bona fide* binding partner of PHLDA2 under physiological settings. Furthermore, we performed an immunofluorescence assay to investigate the intracellular localization of PHLDA2 and ALOX12. We found that PHLDA2 and ALOX12 were co-localized mainly in the cytoplasm (Figure 2E).

PHLDA2 belongs to the Pleckstrin Homology (PH) like domain family A, including PHLDA1, PHLDA2, and PHLDA3 (Figure S2A). Nevertheless, in contrast to PHLDA2, neither PHLDA1 nor PHLDA3 showed any detectable interaction with ALOX12 under the same conditions (Figures 2F, S2B, and S2C). To further ascertain the direct interaction between PHLDA2 and ALOX12, we performed *in vitro* GST pull-down assays and found ALOX12 strongly bound the GST-PHLDA2 fused proteins but not GST alone (lane 2 vs 3, Figure 2G). More specifically, ALOX12 bound a GST-fusion protein harboring the N-terminal PH domain (amino acids 7–101) but not the C-terminal domain (ΔPH, amino acids 102–152) (lane 4 vs 5, Figures 2G and S2D). Similar results were also obtained by the co-immunoprecipitation assay when SFB-tagged PHLDA2, PH, or ΔPH was co-expressed with ALOX12 in H1299 cells (Figures S2D and S2E). Moreover, the well-conserved phospholipids Binding Sequences of PHLDA2 (BS, amino acids 7–31) were not required for interacting with ALOX12, but a small region next to that (ΔBS, amino acids 32–101) was the major docking site for ALOX12 (Figures S2D and S2F). These results demonstrate the specific direct interaction between PHLDA2 and ALOX12.

Since both ALOX12 and PHLDA2 are critical for the ferroptotic responses upon high levels of ROS, to elucidate the functional consequence of this interaction, we examined whether PHLDA2 is required for ALOX12-dependent ferroptosis. To this end, we established isogenic lines of doxycycline-inducible ALOX12 U2OS cells (ALOX12-tet-on cells) in which the PHLDA2 gene has or has not been knocked out by CRISPR/Cas9 technology, as confirmed by Western blot analysis (Figure 2H). Indeed, induction of ALOX12 promoted ferroptotic cell death without any effect on other types of cell death upon high levels of ROS (Figures 2I and 2J). However, the levels of ferroptosis induced by ALOX12 were dramatically diminished upon loss of PHLDA2 (Figures 2I and 2J). The lipid peroxidation levels induced by ALOX12 were also abrogated upon loss of PHLDA2 expression, suggesting that ALOX12-mediated lipid peroxidation and subsequent ferroptosis depends on the presence of PHLDA2 expression (Figure 2K); in contrast, neither ALOX12 overexpression nor loss of PHLDA2 showed any obvious effect on the levels of apoptosis and necroptosis under the same conditions (Figure S2G). Next, we examined whether the

interaction between PHLDA2 and ALOX12 is required for ferroptosis. As expected, the ectopic expression of wildtype PHLDA2 in PHLDA2-null cells restored the ferroptotic responses (Figures S2H and S2I). However, re-expression of the PH domain of PHLDA2 alone required for ALOX12 binding was sufficient to restore the ferroptotic responses; in contrast, expression of the C-terminal domain of PHLDA2 (ΔPH) defective for ALOX12 binding failed to do so (Figures S2H and S2I).

Interestingly, two missense mutations are identified on the ΔBS subdomain of PHLDA2 in the COSMIC database of human tumor specimens: R35H (R→H mutation at amino acid 35) and R46P (R→P mutation at amino acid 46) (Figure S2J). Since the mutated residues are evolutionally conserved and localized within the ΔBS subdomain, these mutations may have functional effects on the PHLDA2/ALOX12 complex. As shown in Figure 2L, the R46P mutation significantly abrogated the binding between ALOX12 and PHLDA2, whereas no pronounced effect was observed for the R35H mutant. Indeed, unlike the PHLDA2 wildtype, the R46P mutant was not very effective in rescuing the ferroptosis activity in the PHLDA2-null cells (Figures 2M, S2K, and S2L). Together, these data indicate that the interaction between PHLDA2 and ALOX12 is essential for ferroptosis induced by high levels of ROS.

PHLDA2 preferentially binds phosphatidic acid (PA) for phospholipid peroxidation

Although the common ferroptotic response is regulated by both GPX4-dependent and GPX4-independent manners, initiation of ferroptosis in cells often requires the treatment of GPX4 inhibitors[1–4]. Using quantitative redox phospholipidomics, Kagan et al. and Doll et al. showed that oxidized forms of only one class of phospholipids, phosphatidylethanolamine (PE), act as the executioners of ferroptosis induced by GPX4 inhibitors[52]. In line with this, contents of oxidatively truncated products of PE are associated with tumor growth *in vivo* GPX4-inactivation-induced tumor model[53]. A systematic redox phospholipidomics analysis of GPX4-inactivation-induced ferroptosis in bone marrow-derived macrophage cells revealed that mainly three phospholipid species (phosphatidylethanolamine, phosphatidylserine, and phosphatidylinositol) contribute to the ferroptotic cell death[54]. Moreover, exogenous PUFA sensitizes cells to GPX4-inactivation-induced ferroptosis by incorporating neutral lipids, including triacylglycerols[55]. It remains unclear how ferroptosis is initiated in the absence of GPX4 inhibition.

Ferroptosis is triggered by excessive peroxidation of the PUFA moieties on membrane phospholipids. ALOX12 is capable of specifically oxidizing free PUFA such as arachidonic acid (AA, C20:4) through its intrinsic lipoxygenase activity[56]. 12-hydroperoxy-AA is the main reaction product (with <5 mol% of 15-hydroperoxy-AA as the minor product) (Figures S3A and S3B). However, the enzyme is less effective in oxygenation of PUFA-phospholipids. Notably, PHLDA2 is a membrane-associated protein with a high affinity for phospholipids[57]. To dissect the precise mechanism by which PHLDA2 regulates ferroptosis, we examined whether PHLDA2 is involved in phospholipids peroxidation by interacting with ALOX12. To this end, we first examined the binding affinity between PHLDA2 and different types of phospholipids. Interestingly, PHLDA2 showed high affinity for PA, phosphatidylserine (PS), phosphatidylinositol (PI) as well as PI phosphorylation derivatives (PIPs) but failed to interact with either PE or phosphatidylcholine (PC), both of which

belong to the most abundant plasma membrane phospholipids (Figure 3A). Moreover, although ALOX12 does not directly bind any of the phospholipids, the ALOX12-PHLDA2 complex showed the same binding pattern as PHLDA2, suggesting that PHLDA2 is able to recruit ALOX12 to specific phospholipids (Figure 3B).

We then purified recombinant PHLDA2 and ALOX12 proteins and employed targeted lipidomics and redox phospholipidomics to examine whether the interaction between PHLDA2 and ALOX12 modulates oxygenation of either free AA or AA-phospholipids, respectively (Figure S3A). PHLDA2 had no obvious effect on ALOX12-mediated AA oxygenation (Figure S3B). Next, we examined the oxygenation activity of ALOX12 and the ALOX12/PHLDA2 complex towards AA-esterified phospholipids: PA, PE, PC, PS, PI, PI(3)P, or PI(3,4)P_2 (referred to as SAPA, SAPE, SAPC, SAPS, SAPI, SAPIP, or SAPIP$_2$). Interestingly, PHLDA2 had significant impacts on ALOX12-mediated lipid peroxidation on different classes of phospholipids (Figures 3C–3F and S3C–S3G). Consistent with its defective binding with PE or PC, PHLDA2 suppressed the activity of ALOX12 to induce the oxidation of SAPE or SAPC; conversely, consistent with its strong binding with PA, PHLDA2 significantly enhanced the activity of ALOX12 to induce the oxidation of SAPA. Nevertheless, no obvious effect of PHLDA2 was detected on SAPS or SAPI. We further examined whether PA-stimulation of peroxidation may be caused by their indirect effects of PHLDA2 and assessed peroxidation of SAPE by the ALOX12/PHLDA2 complex in the presence of one type of non-oxidizable PA, di-palmitoyl-PA (di-PP-PA). The latter did not significantly affect the peroxidation of SAPE by the complex (Figure S3H).

Previous studies showed that oxygenation of PUFA-PE was the executioner of ferroptosis induced by GPX4 inhibitors, while our data suggest oxygenation of PUFA-PA could be the other executioner of ferroptosis. To this end, we tested whether oxygenation of SAPA by the ALOX12/PHLDA2 directly stimulates ferroptosis in the absence of ferroptosis inducers. To avoid any indirect effect on the GPX4/ACSL4 pathway, we generated SAPA:DOPC liposomes and incubated the particles within GPX4/ACSL4 double knockout cells (Figure 3G). Indeed, high levels of ferroptosis were induced by SAPA upon co-expression of PHLDA2 and ALOX12 (Figure 3H). These data indicate that the oxygenation of PUFA-PA by the PHLDA2/ALOX12 complex is capable of initiating ferroptosis without any treatment of common ferroptosis inducers.

Oxidation of phosphatidic acid (PA), but not phosphatidylethanolamine (PE) is critical for ROS-induced ferroptosis

1-acyl-sn-glycerol-3-phosphate O-acyltransferase (AGPATs) are a family of enzymes that catalyze the conversion of lysophosphatidic acid (LPA) to phosphatidic acid (PA) critical for subsequent biosynthesis of other classes of phospholipids including PE, PC, PS, and PI. Although the different AGPAT isoforms catalyze the same reaction, they appear to have unique non-overlapping roles, possibly determined by their substrate specificity. The essential role of LPCAT3 in the biosynthesis of PUFA-PE and ferroptosis is well established; recent studies also showed that 1-acyl-sn-glycerol-3-phosphate O-acyltransferase gamma (AGPAT3) is also critical for the biosynthesis of PUFA-PE[39]. Our

data suggest that PHLDA2-induced ferroptosis is mediated by phosphatidic acid (PA) oxidation, not by peroxidation of phosphatidylethanolamine (PE).

To this end, we compared the results from the CRISPR-Cas9 knockout screens by treating the cells with RSL-3 or high levels of ROS (generated by TBH), respectively (Figure S4A). As expected, both *ACSL4* and *AGPAT3* were selected as the top candidates as key positive regulators in the ferroptosis induced by RSL-3, although neither of them was found to have any effect in the ferroptosis induced by TBH. In contrast, *GPAT3* (Gene ID: 84803) was identified as a potential positive regulator only in the ferroptosis induced by TBH (β score 0.41, p=0.0041)[58, 59]. Meanwhile, no other PA synthesis-related genes, including diacylglycerol kinases and the phospholipase D enzymes, were identified as pro-ferroptotic hit upon these two treatments (Figure S4B)[60]. To examine the distinct effects of GPAT3 and APGAT3 in ferroptosis, we generated A375-derived AGPAT3-null or GPAT3-null cells (Figures 4A and S4C). Indeed, AGPAT3-null cells were resistant to the ferroptosis induced by RSL-3 but not TBH (Figures S4D and S4E). Conversely, loss of GPAT3 expression significantly abrogated the ferroptosis induced by TBH or cystine starvation but not RSL-3 (Figures 4B, 4C, and S4F–S4I). Moreover, ectopic expression of GPAT3 in GPAT3-null cells restored the sensitivity of those cells to ferroptosis, validating the specific role of GPAT3 in ferroptosis regulation (Figures 4D and 4E). Moreover, by pre-incubating the GPAT3-null cells with SAPA:DOPC liposomes, the ferroptotic response induced by TBH or cystine starvation was also totally restored (Figures S4J–S4L), suggesting a critical role of GPAT3 in the biosynthesis of PUFA-PA and ferroptosis induction. Given that AGPAT3 and GPAT3 are interconnected within the same PA synthesis pathway, it is essential to address the reason for their distinct effects in ferroptosis. To this end, we first analyzed the effects of PA contents in the presence or absence of AGPAT3 (Figure S4M). Previous studies showed that AGPAT3 is critical for the ferroptotic response induced by GPX inhibitors through modulating the levels of PUFA-PE[39]. Interestingly, our lipidomics analysis revealed that loss of AGPAT3 had no pronounced effects on the contents of PUFA-PA species (Figures S4N and S4O). Thus, AGPAT3 is required for the synthesis of PUFA-PE but dispensable for the synthesis of PUFA-PA.

Next, to directly examine the effect of GPAT3 on the biosynthesis of PUFA-PA and lipid peroxidation, we performed the phospholipidomics and redox phospholipidomics analysis in both control and GPAT3-null cells upon TBH treatment in the absence or presence of ferrostatin-1 (Ferr-1). We found the levels of PA, especially PUFA-PA, were markedly reduced upon loss of GPAT3 expression (Figures 4F, 4G, and S5A); in contrast, no significant effects on the levels of PC and PE were detected (Figures 4H, 4I, S5A, and S5B). Specifically, as shown in Figure 4G, in wildtype cells, the contents of non-oxygenated PUFA-PA species significantly declined upon TBH treatment, whereas GPAT3 depletion completely abrogated this phenomenon, suggesting the rapid consumption of PUFA-PA upon TBH-induced lipid peroxidation. Consistently, the levels of PA(36:2)+2O, the major oxygenated form of PUFA-PA was dramatically upregulated upon TBH treatment, and this stimulation was abolished by Ferr-1 (Figures 4J, S5C, and S5D). This upregulation was completely abolished in the isogeneic GPAT3-null cells under the same treatments (Figures 4J and S5D). In contrast, oxygenation levels of PE and PC were stimulated both in WT and GPAT3 knockout cells (Figures 4K, 4L, and S5E). These data indicate that, unlike AGPAT3,

GPAT3 is dispensable for the synthesis of PUFA-PE but critical for the biosynthesis of PUFA-PA, which is required for ferroptosis induction under high levels of ROS.

PHLDA2-mediated ferroptosis is required for tumor suppression in immunodeficient mouse models.

Notably, cancer cells rewire cellular metabolism to meet the energetic and substrate demands of tumor development, but this rewiring also creates metabolic vulnerabilities specific to cancer cells[61]. For example, to fuel their enhanced growth and proliferation, neoplastic cells undergo metabolic reprogramming, typically by enhancing glycolytic function and dampening oxidative phosphorylation, generally accompanied by increased ROS production[62–64]. Thus, the levels of ROS are much higher in cancer cells than in normal cells, which may make the cancer cells more susceptible to ROS-induced ferroptosis.

Since the upregulation of tumor growth is mainly affected by either increasing cell proliferation or suppression of cell death, we first examine whether PHLDA2 has any effect on cell proliferation. As shown in Figure S6A, neither loss of PHLDA2 nor loss of ACSL4 had an obvious effect on cell proliferation. Next, we tested whether PHLDA2 has any effect on tumor growth *in vivo* by using immunodeficient mouse models in the absence of any common ferroptosis inducer treatment. Strikingly, the growth of A375 xenograft tumors was dramatically enhanced upon loss of PHLDA2 expression, whereas loss of ACSL4 expression showed no notable change (Figures 5A, 5B, and S6B). Interestingly, the levels of *PTGS2*, a well-known ferroptosis marker, were down-regulated in PHLDA2-null tumors in comparison to control tumors or ACSL4-null tumors (Figure 5C). Moreover, by analyzing the lipid peroxidation levels of tumor section by 4-HNE immunohistochemical (IHC) staining, we found significantly decreased 4-HNE levels in PHLDA2-null tumors but not ACSL4-null tumors (Figures 5D and 5E). To validate these findings, we performed the same experiments with human lung carcinoma A549 cells. Again, we found that loss of PHLDA2 but not loss of ACSL4 promotes the tumor growth of A549-derived xenograft models (Figures S6C–S6F).

To further elucidate whether ferroptosis is indeed involved in the PHLDA2-mediated effect in tumor growth, we used fresh tumor samples to examine the lipid peroxidation levels of tumor-derived live cells by flow cytometry. PHLDA2-null, but not ACSL4-null tumor cells, displayed significantly reduced levels of lipid peroxidation (Figure 5F). In contrast, cleaved caspase 3 staining and Ki67 staining assays showed no obvious difference among these tumors, suggesting that neither apoptosis nor cell proliferation contributes to PHLDA2-mediated tumor suppressive effect (Figures 5G, 5H, and S6G–S6L). Of note, ACSL4 is essential for ferroptosis induced by GPX4 inhibition. Since all the mice bearing different tumors were not treated by any compound, including GPX4 inhibitors, it is not surprising that no effect on ferroptosis or tumor growth was detected upon loss of ACSL4.

Finally, we examined whether the ferroptosis activity that occurred in the tumors expressing PHLDA2 is required for tumor suppression. To do so, we tested whether the tumor growth suppression effects could be reversed in the presence of the ferroptosis inhibitor. Indeed, as shown in Figures 5I and 5J, upon the treatment of ferrostatin-1, the growth suppression in the tumors expressing PHLDA2 was significantly abrogated, very similar to the effects

induced by loss of PHLDA2 expression as shown above (Figure 5A); however, the growth-promoting effects of ferrostatin-1 were not observed in the tumors derived from PHLDA2-null cells, underscored the specific role of PHLDA2-dependent ferroptosis (Figures 5I and 5J). As expected, high levels of lipid peroxidation were detected in the fresh tumors derived from the control group, but the levels significantly declined upon the ferrostatin-1 treatment or loss of PHLDA2 expression (Figure 5K). To corroborate with these findings, we performed the same assays using A549-derived or MCF7-derived immunodeficient tumor models under the same conditions. Indeed, similar data were obtained to produce the same conclusion (Figures S6M–S6R). Taken together, these data suggest that PHLDA2-mediated ferroptosis is critical for tumor growth by using the xenograft tumor models in immunodeficient mice. Our study also reveals that PHLDA2-mediated ferroptosis occurs naturally *in vivo* in the absence of the treatment of any ferroptosis inducers.

PHLDA2-mediated ferroptosis is crucial for tumor suppression in the immunocompetent mice

Although numerous studies indicate that the common ferroptosis response induced by GPX4 inhibitors is dependent on the levels of ACSL4, hepatocyte-specific inactivation of the *ACSL4* gene does not promote tumorigenesis; instead, reduces tumor formation in a liver cancer tumor model[40]. Since PHLDA2-mediated ferroptosis is ACSL4-independent, we applied the well-established carcinogen-induced hepatocellular carcinoma (HCC) model to investigate the effects of PHLDA2-mediated ferroptosis in tumor development. To this end, *Phlda2* wild-type or homozygote knockout mice of the same age were injected weekly with the chemical carcinogen diethylnitrosamine (DEN). After 8-weeks-injection, mice were kept for an additional 27 weeks before analysis of HCC progression (Figure 6A). Both $Phlda2^{+/+}$ and $Phlda2^{-/-}$ mice had developed multiple tumors, suggesting the DEN-induced HCC model was successfully established (Figures 6B–6D). Strikingly, the size of the tumors per animal and overall tumor burden were dramatically increased upon loss of *Phlda2* (Figures 6E and 6F). To examine whether ferroptosis is involved in the PHLDA2-mediated tumor suppressive effects, we collected tumor samples from the largest tumor per mouse and examined the mRNA levels of ferroptosis markers, *Ptgs2* and *Chac1*. Indeed, a significant reduction of *Ptgs2* and *Chac1* mRNA levels was detected, indicating that loss of ferroptosis induction contributes to tumor growth in the HCC model (Figure 6G).

Finally, to further evaluate the role of PHLDA2 in tumor suppression, we tested whether loss of PHLDA2 expression impacts *Myc*-induced tumorigenicity in the classic *Eμ-Myc* lymphoma model. *Eμ-Myc* mice develop late-onset B-cell lymphomas between 6 and 12 months of age; previous studies showed that the loss of one *p53* allele is sufficient to reduce the latency of tumor formation[65]. Interestingly, we observed that the latency of tumor formation in *Eμ-Myc* mice (median overall survival around 195 days) was significantly reduced by the loss of one *Phlda2* allele ($Phlda2^{+/-}$; *Eμ-Myc* mice; median overall survival around 120 days) (Figures 6H and S6S). Although the *Phlda2* gene did not show a loss of heterozygosity (LOH) event in tumors, further analysis showed that the loss of one *Phlda2* allele significantly reduces the mRNA levels of *Phlda2* in the tumors (Figures S6T and S6U). In addition, no obvious alterations were detected for other known factors normally involved in the p53 pathway, including MDM2, MDMX, ARF, and p53 (Figure

S6V), indicating that loss of PHLDA2-mediated ferroptosis contributes significantly to tumor development. Again, the levels of the ferroptosis markers, *Ptgs2* and *Chac1*, were significantly decreased in the tumors of *Phlda2*$^{+/-}$; *Eμ-Myc* mice in comparison to the tumors of *Eμ-Myc* mice (Figure 6I). Taken together, these data demonstrate that PHLDA2-mediated ferroptosis is crucial for tumor suppression in mice with intact immune systems.

Discussion

Numerous studies indicate that ferroptosis is a new tumor suppression mechanism with promising therapeutic potentials[1–4]. The canonical ferroptosis response is well accepted as the cell death induced by inhibiting GPX4 activities[66]. Although the role of ferroptosis in killing tumor cells is well established in tissue cultures as well as xenograft tumor models in immunodeficient mice, this notion has been challenged by recent studies showing that ferroptosis induction promotes tumor growth potentially through sabotaging the anti-tumor immunity in immunocompetent mice[32, 33, 40, 67]. In this study, we discovered a new type of ferroptosis mediated by a phospholipid-binding protein PHLDA2 and demonstrated that PHLDA2-mediated ferroptosis occurs naturally *in vivo* critically for tumor growth in both immunodeficient and immunocompetent environments.

It is well established that the canonical ferroptosis response induced by GPX4 inhibitors is mainly controlled by ACSL4. Subsequent studies by Kagan et al. and Doll et al. provided the precise mechanism of ferroptosis initiation by showing that oxidized forms of PUFA-PE are the major executioners of ferroptosis induced by GPX4 inhibitors[52, 68]. Thus, it is very likely that ACSL4-dependent PUFA-PE peroxidation is a part of normal homeostasis that requires detoxification by GPX4 to prevent the cells from ferroptosis. Thus, the ferroptosis response induced by GPX4 inhibitors occurs in most cell types regardless of normal tissues or cancer cells. In contrast, PHLDA2-mediated ferroptosis is independent of the ACSL4-GPX4 axis. PHLDA2, a phospholipid- binding protein, is unable to bind phosphatidylethanolamine but has a strong affinity for phosphatidic acid and promotes its peroxidation upon high levels of ROS. Thus, unlike ACSL4-dependent PUFA-PE peroxidation, PHLDA2-induced peroxidation of PUFA-PA does not occur under normal homeostatic conditions but is significantly induced when high levels of ROS are generated in the cells or the cells are under metabolic stress (e.g., cystine deprivation). Consistent with this notion, both ACSL4 and GPX4 are essential for normal homeostasis, as the knockout of either ACSL4 or GPX4 leads to embryonic lethality[69, 70]. In contrast, knockout of *Phlda2* in mice has no obvious effect in normal tissues[44]. However, the levels of ROS are much higher in cancer cells than in normal cells, which may make the cancer cells more susceptible to ROS-induced ferroptosis. Indeed, loss of PHLDA2 in tumor cells promotes tumor growth by abrogating ROS-induced ferroptosis by using tumor models with both immunodeficient- or immunocompetent mice.

Indeed, it is not surprising that the canonical ferroptotic response mainly governed by the GPX4/ACSL4 axis is widely involved in controlling the growth of both normal (e.g., neutrophils and T cells) and neoplastic cells. In contrast, PHLDA2 is not required for normal homeostasis but is critical for ferroptosis under specific stress conditions. Our data indicate that PHLDA2-mediated PA-PUFA peroxidation provides a secondary line of

lipid peroxidation-induced ferroptosis that only occurs under stressed conditions such as high levels of ROS or metabolic stress. More importantly, tumor cells undergo metabolic reprogramming to fuel their rapid growth, generally accompanied by increased ROS levels and metabolic stress[62–64]. Indeed, our mouse models demonstrate that PHLDA2-mediated ferroptosis occurs naturally in tumor cells in the absence of the treatment of any ferroptosis inducers.

Limitations of the study

Our study indicates that PHLDA2 is critical for ferroptosis by recruiting ALOX12 to promote the peroxidation of phosphatidic acid, a specific type of phospholipid. PHLDA2-dependent ferroptosis induction is critical for tumor suppression in both immunodeficient and immunocompetent mice, suggesting PHLDA2 as the natural defense against cancer development. However, given that PA makes up a small percentage of the plasma membrane, further studies are required to dissect how a relatively small amount of peroxidized PUFA-PA is able to initiate the ferroptotic response *in vivo* effectively. It remains unclear whether peroxidized PUFA-PA alone is sufficient to initiate ferroptosis or might act as a fuse, leading to more wide-spread peroxidation of other types of PUFA-PLs for initiating ferroptosis. Moreover, it is critical to investigate whether PHLDA2 is able to induce peroxidation of PUFA-PA in the membranes of different intracellular organelles besides plasma membranes, including endoplasmic reticulum, peroxisome, Golgi apparatus, or mitochondria. Since ferroptosis was discovered in 2012, most of the studies focuses the canonical ferroptotic response that requires the treatment of GPX4 inhibitors, also known as ferroptosis inducers[1–4]. Notably, our study implicates a distinct pathway for ferroptosis that occurs naturally *in vivo* without any treatment from those common ferroptosis inducers. Future investigations are required to determine which pathway truly represents the physiological checkpoint in tumor suppression.

STAR METHODS

RESOURCE AVALIBITY

Lead contact—Further information and requests for resources and reagents should be directed to and will be fulfilled by the lead contact, Wei Gu (wg8@cumc.columbia.edu).

Materials availability—All the materials generated in this study (see Key resource table) are available upon request from the lead contact. This study did not generate unique reagents.

Data and code availability

- All data reported in this study are available from the lead contact upon request. Uncropped Western blots and all raw data used to generate graphs are uploaded in Mendeley data (http://doi.org/10.17632/6rjv2vwntc.1).
- This paper does not report the original codes.
- Any additional information required to reanalyze the data reported in this paper is available from the lead contact upon request.

EXPERIMENTAL MODEL AND STUDY PARTICIPANT DETAILS

Cell line—Human embryonic kidney HEK293T, human breast cancer MCF-7 (p53 wildtype), human lung adenocarcinoma A549 (p53 wildtype), human bone osteosarcoma U2OS (p53 wildtype), human melanoma A375 (p53 wildtype) and human non-small cell lung carcinoma H1299 (p53 null) cells were previously obtained from ATCC. Cells were cultured with DMEM supplemented with 10% (v/v) FBS (Gibco), 100 units/ml penicillin, and 100 μg/ml streptomycin (Gibco) in a humidified incubator at 37°C and 5% CO_2. To induce the expression of ALOX12 in U2OS cells, culture medium was added with 0.5μg/ml of doxycycline. All cell lines have been regularly tested to be negative for mycoplasma contamination every month. No cell lines used in this work were listed in the ICLAC database. The cell lines were freshly thawed from the purchased seed cells and were cultured for no more than one month. The morphology of cell lines was checked before the experiments and compared with the ATCC cell line image to avoid cross-contamination or misuse of cell lines.

Animals—All the mice were housed in a temperature-controlled room (65–75 °F) with 40–60% humidity, with a light/dark cycle of 12h/12h. All animal experiments were approved by the Institutional Animal Care and Use Committee (IACUC) at Columbia University under the supervision of the Institute of Comparative Medicine (ICM).

Six-week-old female nude mice (Nu/Nu, Charles River) were used for immunodeficient xenograft experiments. Randomization of animals was performed before the xenograft experiments. The tumors in the xenograft experiments did not exceed the limit for tumor burden (10% of total body weight or 2 cm in diameter).

Phlda2 homozygous mice were kind gifts from Dr. Benjamin Tycko. The offspring were PCR genotyped using a primer set (common Forward, 5'- AGAGCCTGCTTGGGATTGAGAGT −3'; wildtype Reverse, 5'- CCTTGTAATAGTTGGTGACGATG −3'; mutated Reverse, 5'-GTCCCAGGAAGTATGATACCTGC −3'). *Eμ-myc* mice were ordered from Jackson Laboratory (Strain #002728). *Eμ-myc* positive mice were genotyped by PCR using forward primer: 5'-TTAGACGTCAGGTGGCACTT-3', and reverse primer: 5'-TGAGCAAAAACAGGAAGGCA-3'. *Eμ-myc* and *Eμ-myc; Phlda2*$^{+/-}$ mice were monitored twice a week for disease state defined by enlarged solid lymph nodes and their date of death was recorded.

Induction of toxic chronic liver injury-induced HCC formation was accomplished as previously described[71]. Briefly, wildtype or *Phlda2*$^{-/-}$ mice received an 8-week intraperitoneal injection of N-Nitrosodiethylamine (Diethylnitrosamine, DEN) at the age of 14 days. DEN was freshly dissolved in 0.9% saline and used at indicated concentrations. The Body weight of the mice was determined at the time of dosing for the intraperitoneal injection. The dosage of DEN for 2-week-old mice, 3-week-old mice, and 4-week-old to 9-week-old mice was 20mg/kg, 30mg/kg, and 50mg/kg, respectively. Mice were sacrificed at 27 weeks after the last dose, after which mice livers were collected for further analysis.

METHOD DETAILS

Genome-wide CRISPR screen and high-throughput sequencing—CRISPR screen was performed in A375 cells. Human lentiviral CRISPR library (H1 and H2) was a gift from Xiaole Shirley Liu (Addgene #1000000132). H2 library contains a total of 92871 sgRNAs for 18436 gene targets with 5 sgRNAs per gene. Library amplification, lentiviral packaging, and titration were all done according to the standard protocol. For transduction, 1.25×10^8 A375 cells (around 400X coverage) were infected with the H2 library at a multiplicity of infection (MOI) of around 0.3. 48h after transduction, T_0 cells were harvested. The rest cells were selected with 0.9 μg/ml puromycin for 48h, and 5×10^7 cells were passaged every 48 – 72 h at a density of 5×10^6 cells for over 14 days. Then, T_{14} cells were harvested. 1×10^8 cells were treated with indicated conditions: 1μM cystine medium for 120h; 0μM cystine medium for 60h; TBH 300μM for 12h; 1μM RSL-3 for 120h. Survived cells each were collected at the endpoint and genomic DNA was isolated using the Wizard Genomic DNA Purification Kit (Promega). The high-throughput sequencing libraries were prepared through two-step PCR amplification. First step, 2.5 μg of genomic DNA was used in a 50μL per PCR reaction of total 96 reactions by Phusion Plus DNA Polymerase (ThermoFisher Scientific). The amplification cycle is 17. PCR primer: Forward P5, 5'-TCGTCGGCAGCGTCAGATGTGTATAAGAGACAGTTGTGGAAAGGACGAAACACCG −3'; Reverse P7, 5'-GTCTCGTGGGCTCGGAGATGTGTATAAGAGACAGCCAATTCCCACTCCTTTCAAGACCT −3'. For the second step, 8 cycles of amplification were done for adding the specific barcode. 75nt reads were done using the Illumina HiSeq2500.

CRISPR screen data analysis.—MAGeCK (version 0.5.7) software was used for screen analysis[43]. Briefly, the resulting sequencing data were de-barcoded, merged, and then the 43 bp single-end reads contained 20-bp sgRNA sequence was aligned to the reference sgRNA library of CRISPR knockout library using 'count' function from MAGeCK without allowing for any mismatches. MAGeCK built a linear model to estimate the variance of guide RNA read counts and evaluated the guide RNA abundance changes between control and treatment conditions. MAGeCK provides a new subcommand, mle algorithm, to calculate gene essentiality from CRISPR screens. MAGeCK-mle was used to detect P value and beta (β) score for positive and negative selection under the method normalizing to the median counts of sgRNAs. The β score is similar to the term guide-level log2 fold change, where a positive beta score means a gene is positively selected, and a negative beta score means a gene is negatively selected.

Plasmid generation, virus packaging, small interfering RNA, and transfection—Human PHLDA2 or GPAT3 isoforms were sub-cloned into pRK5 vectors or NT-GFP Fusion TOPO vectors (ThermoFisher Scientific). Mutant PHLDA2 plasmids were constructed by using the QuickChange XL Site-Directed Mutagenesis Kit (Agilent) according to the standard protocol. pEGFP-TDAG51 (PHLDA1) was a gift from Richard C. Austin (Addgene plasmid # 32699; http://n2t.net/addgene:32699; RRID: Addgene_32699). For SFB-PHLDA2 and SFB-PHLDA3 plasmid, full-length PHLDA2 and PHLDA3 cDNA were amplified from HCT116 cells and then sub-cloned into SFB N-terminal vector.

Full-length PHLDA2 cDNA was also sub-cloned into pLVX-M-puro (Addgene, plasmid #125839). Flag-HA-ALOX12 and SFB-ALOX12 were as described previously[7].

PHLDA2 pLVX plasmids were co-transfected with viral packaging plasmids (psPAX2 and pMD2G) into HEK293T cells according to the ratio of plasmids is 4:3:1 using Lipofectamine 3000 Reagent (Invitrogen, L3000150). After 48 hours transfections, medium of HEK293T cells was collected and filtered with 0.45μm PES filter. Further, U2OS, A549, or A375 cells were infected with vital medium for 12 hours and split into single cells. Cells were selected with 1 μg/mL puromycin for 2 weeks and performed western blot analysis to identify protein overexpressing level.

Transfection of expressing plasmids was conducted by Lipofectamine 3000 Reagent (Invitrogen, L3000150) or Helix-IN DNA Transfection reagent (OZ Biosciences, HX10500) according to the manufacturer's protocol. PHLDA2 siRNA ON-TARGET plus SMARTpool was ordered from Dharmacon (L011411). Transfection with siRNA was performed using Lipofectamine 3000 Reagent for 24h and then transfected again according to the manufacturer's instructions.

Cystine starvation treatment—For cystine starvation medium, glutamine, methionine, and cystine-deficient DMEM (21013024, Invitrogen) was supplemented with 4mM glutamine, 200μM methionine and 10% FBS. For specific cystine containing medium, indicated cystine was added back to cystine starvation medium. Before seeding, cells were pre-washed with PBS 3 times and then split into cystine starvation medium or cystine-containing medium for the indicated time.

Cell viability assay—Unless otherwise specified, cells were seeded in white, sterile, and tissue culture treated opaque 96-well microplate (PerkinElmer) at 5×10^3 cells per well. About 18h after cell seeding, cells were pre-treated with indicated compounds for indicated time before further treatment or directly treated with indicated compounds at the indicated concentrations for indicated time. There were three biological replicates per condition. Cellular ATP levels were quantified using CellTiter-Glo 2.0 reagent (Promega) following the manufacturer's instructions by GloMax Discover Microplate Reader (Promega). Relative cell viability was measured in comparison to the relative untreated condition. Nonlinear regression analysis of the mean ± SD n = 3 biological replicates of each data point was used to measure the fit curves of cell viability by GraphPad Prism 8.0. To calculate the cell death ratio by this method, percentage of cell death was counted as 100 minus percentage of cell viability.

Lactate dehydrogenase (LDH) release assay—Cells were seeded in white, sterile, and tissue culture-treated opaque 96-well microplate at 1×10^4 cells per well. After the indicated treatment, the release of LDH from damaged cells was measured by a CytoTox-ONE Homogeneous Membrane Integrity Assay kit (Promega) according to the manufacturer's instructions. The fluorescence intensity was measured by using the GloMax Discover Microplate Reader. LDH release ratio was calculated by Fluorescence of sample/ Fluorescence of 100% cell lysis positive control.

Cell death assay—Cells were seeded in a 12-well plate (Corning) at 4×10^4 cells per well. About 18h after cell seeding, cells were pre-treated with indicated compounds for the indicated time before further treatment or directly treated with the indicated compounds at the indicated concentrations for indicated time. 30nM SYTOX green dead cell stain was added into plates and incubated for 1h at 37°C. At least three randomly chosen bright-fields and FITC fluorescence-fields were captured by microscopy (Olympus, IX51). Living cells (without green stained) and dead cells (without green stained) were counted, and the cell death ratio was calculated by the Number of dead cells/Number of (living cells + dead cells).

Complex purification and Mass Spectrometry analysis—To generate an ALOX12 stable line, SFB-ALOX12 plasmid was transfected into H1299 cells with Lipofectamine 3000, followed by puromycin (1 μg/mL) selection for 2 weeks and maintenance under puromycin (0.25 μg/mL).

The complex purification processes were described previously[38]. Briefly, the cell pellet was collected and resuspended in Complex Buffer (50mM Tris-HCl pH 7.3, 100mM NaCl, 0.1mM EDTA, 0.2% NP-40, and 10% glycerol) on ice for 3h. After centrifugation, the supernatant was filtered with 0.45μm syringe filters, and was first immunoprecipitated by Streptavidin beads overnight. The bound peptides were eluted by Biotin and were secondly purified by anti-S protein beads overnight. The final elutes by glycine were resolved by SDS-PAGE on a 4%–20% gradient gel and stained by GelCode Blue Stain Reagent. The visible bands were digested with trypsin and then subjected to liquid chromatography-mass spectrometry (LC-MS/MS) analysis at Harvard Center for Mass Spectrometry.

Co-immunoprecipitation (IP) assay—Cells were harvested and rinsed with PBS twice. Cells were lysed with BC150 Buffer (50mM Tris-HCl pH 7.3, 150mM NaCl, 0.1mM EDTA, 0.4% NP-40, and 10% glycerol) added protease inhibitor cocktail, 1mM dithiothreitol (DTT) and 1mM phenylmethyl sulfonyl fluoride (PMSF) on ice for 1h, following sonication for 20s. Cell lysates were centrifuged for 15min at 15000 rpm, and the supernatant was collected. Then, the same total protein quantified with Bio-Rad Protein Assay Dye Reagent (Bio-rad, 5000006) was taken for IP assay. Lysates were added HA agarose or Streptavidin agarose and incubated overnight at 4 °C. Next day, beads were washed with BC200 buffer (same formula as BC150 besides 200mM NaCl) two times and BC150 buffer three times, and the complex was eluted by 1×Loading buffer, 0.1M glycine buffer (pH=2.6), or Biotin for further western blot analysis.

Protein purification—HEK293T cells were transfected with Flag-HA-tagged ALOX12 and Flag-tagged PHLDA2. 48 h after transfection, cells were harvested and lysed in BC500 (same formula as BC150 Buffer besides 500mM NaCl), following sonication for 3min. An appropriate amount of Flag M2 Affinity Gel was added to the supernatant and incubated overnight at 4 °C. Next day, beads were rinsed with BC500 buffer six times and the purified proteins were eluted with Flag peptide diluted in detergent-free BC20 buffer (50mM Tris-HCl pH 7.3, 20mM NaCl, 0.1mM EDTA, and 10% glycerol) several times. Eluted proteins were concentrated by 10kDa Amicon Ultra-0.5 Centrifugal Filter Unit (Sigma-Aldrich, UFC501024). Finally, a certain amount of protein was measured by SDS-PAGE gel and

stained by GelCode Blue Stain Reagent (ThermoFisher Scientific, 24592). Bovine serum albumin proteins (BSA) were used for quantification.

***In vitro* GST pull-down assay—**PHLDA2 full-length or PHLDA2 fragments were sub-cloned into pGEX-4T-2 vectors. GST, GST-PHLDA2 Full-length, GST-PHLDA2-PH or GST-PHLDA2-ΔPH proteins were inducible expressed in *Rosetta* bacterial cells and incubated with GST Bind Resin (Novagen, 70541). GST-tagged protein was eluted with glutathione several times. Equal amounts of purified Flag-HA tagged ALOX12 were incubated with equal amounts of corresponding GST-tagged proteins in BC200 (same formula as BC150 Buffer besides 200mM NaCl) buffer for 4 h at 4 °C, followed by washing with BC200 buffer six times. The binding complex was eluted by boiling with 1×Loading buffer for western blot analysis.

Western blot and antibodies—Cells were lysed with Flag lysis buffer [50mM Tris-HCl (pH 7.9), 137mM NaCl, 1% Triton X-100, 0.2% Sarkosyl, 1mM NaF, 1mM Na_3VO_4, and 10% glycerol] containing protease inhibitor cocktail and 1mM DTT, and 1mM PMSF. The same amount of protein from different experiment groups was quantified and detected with western blot analysis. Western blot was conducted for protein analysis according to standard methods with 4%−20% pre-cast SDS–PAGE gel (Invitrogen, XP0420). Commercial antibodies is shown in Key resources table. Horseradish peroxidase-conjugated goat anti-mouse and anti-rabbit secondary antibody (Jackson ImmunoResearch) and anti-rat (Southern Biotech) were used.

Immunofluorescence staining—U2OS cells were seeded into glass coverslips in 6-well plates and washed with PBS three times. Then, cells were fixed with 4% formaldehyde in PBS for 20 min and permeabilized with 0.2% Triton X-100 in PBS for 20 min at room temperature. After rinsing with washing buffer (0.1% Triton X-100 in PBS) three times, the cells were blocked for 2h with blocking buffer (5% BSA and 5% goat serum in washing buffer) and incubated with anti-ALOX12 (1:10 dilution) and anti-PHLDA2 (1:50 dilution), antibodies in blocking buffer overnight in 4°C. The next day, the cells were rinsed with washing buffer four times and incubated with Alexa Fluor 488 goat anti-rabbit secondary antibodies and Alexa Fluor 568 goat anti-mouse secondary antibodies (1:2000 in the blocking buffer) at room temperature for 1h. Glass coverslip was mounted onto glass slides with Antifade Mounting Medium with DAPI (VECTASHIELD, H1200). Images were visualized with an Olympus IX51 microscope.

qRT-PCR—Total RNA was isolated using TRIzol reagent (Invitrogen) according to the manufacturer's instructions. cDNA was reversed by SuperScript IV VILO Master Mix (Invitrogen). qPCR was then performed using SYBR Green Master Mix (Invitrogen) to detect the mRNA expression levels of indicated genes. The expression levels of target genes were normalized by *GAPDH* or *Actin*. The following primers for human genes and mouse genes were shown in Key resources table.

CRISPR-Cas9 system-mediated gene ablation—p53 knockout cells were previously described. To produce PHLDA2, ACSL4, GPX4, AGPAT3, and GPAT3 sgRNAs expressing cell lines, indicated cells were co-transfected gene TrueGuide Synthetic guide RNA

(Invitrogen, A35533) or Negative Control non-targeting RNA (Invitrogen, A35526) with TrueCut Cas9 protein v2 by Lipofectamine CRISPRMAX Transfection Reagent. After 48 h transfection, pooled cells were seeded for cell viability or western blot validation, and the rest of the cells were split into single cells for colony culture and further analysis. AGPAT3 sgRNAs were designed by CRISPOR[72] and synthesized by Synthego. Other sgRNAs were directly purchased from Invitrogen. The sgRNA sequence or sgRNA catalog number purchased from Invitrogen were shown in Key resources table.

Cell count assay—For cell counts and cell double time calculation, NC, PHLDA2$^{-/-}$, or ACSL4$^{-/-}$ A375 cells were seeded at 8×10^4 cells per well in 6 well plates. Plates were incubated at 37°C, 5% CO_2 for 120h. Total cells were digested by trypsin, collected, and counted with a hemocytometer using the standard protocol. Cell doubling time was calculated by $120/\log_2$[(Final cell numbers/Initial cell numbers)].

PIP Strips Dot blot assay—PIP Strips (Echelon Biosciences) were used to assess the phospholipids-binding properties of PHLDA2 and ALOX12. The membrane was blocked in 3% fatty acid-free BSA in TBST overnight at 4°C. The membrane was then incubated with recombinant PHLDA2 proteins (0.25μg/ml) or ALOX12 proteins (0.25μg/ml) in 3% BSA containing TBST for 2 hours at room temperature with gentle stirring. Membranes were washed three times for a total of 20 min in TBST and then incubated with indicated antibody in 3% BSA-containing TBST overnight at 4°C. The membranes were washed as before, then incubated with the secondary antibody of horseradish peroxidase conjugate with 1:5000 dilution in 3% BSA containing TBST for 1h at room temperature. Finally, the membranes were washed as before, and the binding signals were detected by K-TMB Precipitating (Echelon Biosciences).

Oxidation of AA and AA-containing phospholipids induced by ALOX12 and/or PHLDA2—Liposomes comprised of AA and AA-containing phospholipids with DOPC (1:1 ratio) were prepared. Briefly, DOPC and lipids were dried in a test tube under inert gas (using a gentle stream of ultra-high purity nitrogen) and then resuspended in buffer [25mM Hepes buffer, pH 7.4, 100μM diethylenetriaminepentaacetic acid (DTPA)] to achieve a final lipid concentration of 100μM. In the experiment with di-PP-PA, the named phospholipid was added to the initial SAPE/DOPC lipid mixture to achieve a final di-PP-PA concentration of 270μM. The suspension was shaken vigorously and extruded through a polycarbonate membrane with 100nm pores. To prevent the conversion of lipid hydroperoxides to secondary products during incubation, the HEPES buffer was saturated with oxygen. Lipoxygenase activity was assessed by the formation of primary products of AA or AA-containing phospholipid oxidation. To do this, liposomes were incubated with recombinant ALOX12 (0.08μM) and/or recombinant PHLDA2 (0.27μM) in the presence of H2O2 (0.5μM) for 5 min at 37°C with stirring. Then lipids (AA, SAPE, SAPC, SAPS, SAPI, SAPA) were extracted twice by adding a mixture of chloroform and methanol (Folch procedure) and analyzed by LC-ESI-MS/MS. LC-ESI-MS/MS analysis was performed on a Thermo Ultimate 3000 HPLC system coupled to a hybrid quadrupole-orbitrap mass spectrometer (Q-Exactive, ThermoFisher Scientific) with an Xcalibur operating system. The instrument was operated in negative ion mode at a voltage differential of −4.0 kV and

source temperature of 320°C. Sheath gas and s-lens were set at 20 and 65, respectively. The resolution was set at 140000 with a scan range of m/z 150–1800 and a user-defined mass tolerance of 5ppm. m/z values for the oxidized species are presented in 4 decimal places. MS/MS was performed in data-dependent mode with HCD fixed at 24 and a resolution of 17,500. Non-oxidized and oxidized lipids were separated on a reverse phase Accucore C30 column (2.6μm, 250 × 2.1mm (ThermoFisher Scientific)) at a flow rate of 0.1mL/min. The column was eluted using a gradient solvent system consisting of mobile phase A (acetonitrile/water, 50/50 v/v) and mobile phase B (2-propanol/acetonitrile/water, 85/10/5 v/v). Both mobile phases contained 5 mM ammonium formate and 0.1% formic acid. The gradient was performed as follows: 30%−70% B, 0–20 min; 70%−100% B, 20–55 min; 100% B, 55–70; 100%−30% B, 70–85 min; 30% B, 85–95 min for equilibration of the column. All gradients were linear.

Phosphatidylinositol Phosphates extraction and LC-ESI-MS/MS analysis— Oxidized Phosphatidylinositol Phosphates (PIPs) were extracted from the sample by the modified procedure[73]. Briefly, to each 100μl of the test sample, 152μl of cold methanol and 1.52μl 12M HCl were added, vortexed for 30 s (repeated 5 times), and placed on ice. Then, 1.13ml chloroform and 400μl of methanol/12M HCl (100:1, v/v) were added, vortexed for 30s and visually checked to make sure that a single-phase system was formed. Samples were left on ice for 1 hour, followed by the addition of 340μl of 0.8M HCl/5mM EDTA/1.76% KCl and vortexed. After separation into 2 phases, the lower organic phase was collected. The upper phase was re-extracted with 1.0 mL of chloroform plus 0.12mL methanol/12M HCl (100:1, v/v). Lower phases were combined, and the pH adjusted to near neutral with NH_4OH. After extraction, oxidized PIPs were dried under N_2 and re-dissolved in chloroform: methanol: H_2O (3:2:1). LC-ESI-MS/MS analysis was performed on a Thermo HPLC system coupled to a hybrid quadrupole-orbitrap mass spectrometer (Q-Exactive, ThermoFisher Scientific) with an Xcalibur operating system. The instrument was operated in negative ion mode at a resolution of 140,000 with a scan range of m/z 150–1800 for the full MS scan at a voltage differential of −3.5 kV and source temperature of 320°C. Sheath gas and s-lens were set at 10 and 60, respectively. A user-defined mass tolerance was set to 5ppm. m/z values for the oxidized species are presented in 4 decimal places. MS/MS was performed in data-dependent mode with HCD fixed at 24 and a resolution of 17,500. Non-oxidized and oxidized PIPs were separated on a reverse phase Luna C18 column (3.0μm, 150 × 1.0mm (Phenomenex, Inc.)) at a flow rate of 0.08 mL/min. The column was eluted using a gradient solvent system consisting of mobile phase A (water, containing 0.1% TEA and 0.03% acetic acid, v/v) and mobile phase B (acetonitrile, containing 0.1% TEA, v/v). The gradient was as follows: 0–4 min, 38–42 %B; 4–6 min, 42–43 %B; 6–7 min, 43–95 %B; 7–9 min, hold at 95 %B; 9–12 min, 95–38 %B; 12–15 min, equilibrate at 38 %B. All gradients were linear.

Phospholipodomics and redox phospholipodomics LC-MS/MS analysis— Lipids from NC or sgGPAT3 A375 cells were extracted using the Folch procedure, and phosphorus was determined by a micro-method as described previously[52]. Phospholipids were analyzed by LC-ESI-MS/MS using a Thermo Ultimate 3000 HPLC system coupled on-line to an Orbitrap Fusion Lumos mass spectrometer (ThermoFisher) using a normal

phase column (Luna 3 μm Silica (2) 100 Å, 150×1.0 mm, (Phenomenex)). The analysis was performed using gradient solvents (A and B) containing 10mM ammonium formate at a flow rate of 0.065 ml/min. Solvent A contained isopropanol/hexane/water (285:215:5, v/v/v), and solvent B contained isopropanol/hexane/water (285:215:40, v/v/v). All solvents were LC/MS-grade. The gradient was as follows:0–3 min, 10–37 %B; 3–15 min, hold at 37 %B; 15–23 min, 37–100 %B; 23–75 min, hold at 100 %B; 75–76 min, 100–10 %B; 76–90 min, equilibrate at 10 %B. Analysis was performed in negative ion mode at a voltage differential of −3.5kV. Resolution was set at 140,000 with a scan range of m/z 400–1800 for the full MS scan using sheath and aux gases set at 35 and 17, respectively. MS/MS was performed by HCD (fixed at 24) in a data-dependent mode at a resolution of 15,000. Analysis of raw LC/MS data was performed using Compound Discoverer™ 2.0 software (ThermoFisher) with an in-house generated analysis workflow and oxidized PL database. Briefly, peaks with S/N ratio of more than 3 were identified and searched against oxidized phospholipids database. Lipids were further filtered by retention time and confirmed by a fragmentation mass spectrum. Values for m/z were matched within 5 ppm to identify the lipid species. Peak areas were used for quantification of oxygenated phospholipids species. Deuterated phospholipids (Avanti Polar Lipids) were used as internal standards. Data were presented as pmol normalized to nmol or μmol of total phospholipids.

Lipid peroxidation analysis using C11-BODIPY—Cells were seeded in a 6-well plate at 12×10^4 cells per well. About 18h after cell seeding, cells were pre-treated with indicated compounds for the indicated time before further treatment or directly treated with indicated compounds at the indicated concentrations for the indicated time. Cells were incubated with 2μM BODIPY™ 581/591 C11 dye for 30min at 37°C. Then, cells were harvested and washed by PBS twice and resuspended in 500μL PBS for flow cytometry analysis. The lipid peroxidation ratio was analyzed using an Attune NxT Acoustic Focusing Cytometer (Thermo Fisher Scientific) by analyzing 10,000 cells.

Tumor tissues were isolated from mice and immersed in PBS. Tumor tissues were then minced into small enough pieces and digested with collagenase type I (Thermo Fisher Scientific, 17100017) at 37°C with intermittent mixing. After 1h incubation, minced tissues looked like a goopy mess and were pipetted to make live cells into single cells with gentle mechanical force. Then, RBC lysis buffer (Biolegend, 420301) was used to eliminate the interference from red blood cells. Further, cells were strained with a 35 μm cell strainer, washed with PBS twice, and stained with 2μM BODIPY 581/591 C11 dye for 25 minutes at 37°C. Then, the stained cells were washed with PBS and resuspended PBS for analysis. The lipid peroxidation ratio was measured with an Attune NxT Acoustic Focusing Cytometer (Thermo Fisher Scientific) by analyzing 10,000 cells.

Immunohistochemical (IHC) staining—Tumor samples were fixed in 10% formalin for 24h and 70% ethanol before being subjected to standard dehydration processing for preparing the paraffin blocks. Paraffin blocks were sectioned at 4μM thickness for IHC staining. Tissue sections were deparaffinized with xylene and followed with gradient ethanol (100%, 95%, 90%, 80%, and 70%). After rinsing with deionized water for 5 min, the sections were incubated in 3% hydrogen peroxide for 20 min to eliminate endogenous

peroxidase. To retrieve antigen, the sections were incubated in 10 mM sodium citrate buffer (pH 6.0) at 100°C for 20min. Then the specimens were washed with PBS three times and incubated with 4-HNE antibody (Abcam, ab46545, 1:200), cleaved caspase 3 antibody (Cell Signaling Technology, 9661, 1:200), or Ki67 antibody (Abcam, ab15580, 1:400) at 4 °C overnight. The next day, the specimens were rinsed with PBS three times, followed by applying the the ImmPRESS HRP Horse Anti-Rabbit IgG Polymer Detection Kit (MP-7401, Vector laboratory). Finally, ImmPACT DAB Substrate Kit (SK-4105, Vector laboratory) was used to detect the signal. The immunohistochemistry images were photographed in microscopy (Eclipse Ni-U, Nikon), and staining scores for each specimen were performed by Image-pro plus software by calculating the relative IOD/Area ratio.

SAPA: DOPC liposome preparation—The equal molar mass of SAPA and DOPC chloroform-solved phospholipids were mixed in a dry vial and then evaporated under a vacuum to yield a thin film on the vial wall. The lipid film was then resuspended in PBS, yielding a 400μM lipid suspension. The lipid suspension was subjected to 3 times of 5min dry ice freezing, 5-minutes room temperature thawing, and 1-minute sonication cycle. The lipid suspension was then extruded 25 times using a mini extruder (Avanti Polar Lipids, 610000) equipped with a 100 nm polycarbonate membrane to form even liposomes.

Xenografts experiments—Cells resuspended with sterile PBS were mixed with Matrigel (Corning) at a 1:1 ratio (volume) and injected subcutaneously into nude mice. 4.0×10^6 cells were used for the xenograft of A549 cells. 3.0×10^6 cells were used for the xenograft of A375 cells. Mice were euthanized 3 weeks after injection, and tumors were dissected and weighed.

For xenograft of A375, A549, or MCF7 cells without or with ferrostatin-1 treatment, 3.0×10^6 of A375 cells, 4.0×10^6 of A549 cells, 4.0×10^6 of MCF7 cells were used. Treatments with ferrostatin-1 started 3 days after injection. Ferrostatin-1 at 1mg/kg per day per mouse was administered intraperitoneally for 14 continuous days. 11 days after ferrostatin-1 treatment (a total of 4 weeks from tumor injection), mice were euthanized, and tumors were dissected and weighed.

Quantification, statistics, and reproducibility—All experiments were independently repeated three times, as stated in Figure Legends. A two-tailed unpaired Student's *t*-test by GraphPad Prism 8.0 was done for the statistical analyses without specific statements. Data represented in the figures were shown with an error of the mean (mean ± SD) without specific statements. $p < 0.05$ was considered statistically significant between groups. Flow cytometry data were analyzed by FlowJo. Data were graphed using GraphPad Prism 8.0.

Supplementary Material

Refer to Web version on PubMed Central for supplementary material.

Acknowledgements

This work was supported by the National Cancer Institute of the National Institutes of Health under Award R35CA253059, RO1CA258390, and R01CA254970 to W.G., and R35CA209896 to B.R.S., and R01CA204232,

R01CA258622, and R01CA166413 to X.J. V.E.G and H.B were supported by AI156924, AI156923, NS061817, NS076511, CA165065, CA266342, and CA243142. We acknowledge the support from the Herbert Irving Comprehensive Cancer Center (HICCC; P30 CA13696) and NCI cancer center core grant P30 CA008748 to MSKCC, and thank the HICCC's shared resources: molecular pathology, flow cytometry, and specialized microscopy. The content is solely the responsibility of the authors and does not necessarily represent the official views of the National Institutes of Health.

References

1. Hadian K, and Stockwell BR SnapShot: ferroptosis. Cell 181, 1188–1188. e1181 (2020). [PubMed: 32470402]
2. Dixon SJ, and Pratt DA Ferroptosis: A flexible constellation of related biochemical mechanisms. Molecular Cell 83, 1030–1042 (2023). [PubMed: 36977413]
3. Chen X, Kang R, Kroemer G, and Tang D Broadening horizons: the role of ferroptosis in cancer. Nature reviews Clinical oncology 18, 280–296 (2021).
4. Lei G, Zhuang L, and Gan B Targeting ferroptosis as a vulnerability in cancer. Nature Reviews Cancer, 1–16 (2022). [PubMed: 34848861]
5. Ubellacker JM, Tasdogan A, Ramesh V, Shen B, Mitchell EC, Martin-Sandoval MS, Gu Z, McCormick ML, Durham AB, and Spitz DR Lymph protects metastasizing melanoma cells from ferroptosis. Nature 585, 113–118 (2020). [PubMed: 32814895]
6. Jiang L, Kon N, Li T, Wang S-J, Su T, Hibshoosh H, Baer R, and Gu W Ferroptosis as a p53-mediated activity during tumour suppression. Nature 520, 57–62 (2015). [PubMed: 25799988]
7. Chu B, Kon N, Chen D, Li T, Liu T, Jiang L, Song S, Tavana O, and Gu W ALOX12 is required for p53-mediated tumour suppression through a distinct ferroptosis pathway. Nature cell biology 21, 579–591 (2019). [PubMed: 30962574]
8. Su Z, Kon N, Yi J, Zhao H, Zhang W, Tang Q, Li H, Kobayashi H, Li Z, and Duan S Specific regulation of BACH1 by the hotspot mutant p53R175H reveals a distinct gain-of-function mechanism. Nature Cancer, 1–18 (2023). [PubMed: 36721073]
9. Jennis M, Kung C-P, Basu S, Budina-Kolomets A, Julia I, Leu J, Khaku S, Scott JP, Cai KQ, and Campbell MR An African-specific polymorphism in the TP53 gene impairs p53 tumor suppressor function in a mouse model. Genes & development 30, 918–930 (2016). [PubMed: 27034505]
10. Gnanapradeepan K, Indeglia A, Stieg DC, Clarke N, Shao C, Dougherty JF, Murali N, and Murphy ME PLTP is a p53 target gene with roles in cancer growth suppression and ferroptosis. Journal of Biological Chemistry 298 (2022).
11. Gnanapradeepan K, Basu S, Barnoud T, Budina-Kolomets A, Kung C-P, and Murphy ME The p53 tumor suppressor in the control of metabolism and ferroptosis. Frontiers in endocrinology 9, 124 (2018). [PubMed: 29695998]
12. Yang X, Wang Z, Zandkarimi F, Liu Y, Duan S, Li Z, Kon N, Zhang Z, Jiang X, and Stockwell BR Regulation of VKORC1L1 is critical for p53-mediated tumor suppression through vitamin K metabolism. Cell Metabolism 35, 1474–1490. e1478 (2023). [PubMed: 37467745]
13. Zhang Y, Shi J, Liu X, Feng L, Gong Z, Koppula P, Sirohi K, Li X, Wei Y, and Lee H BAP1 links metabolic regulation of ferroptosis to tumour suppression. Nature cell biology 20, 1181–1192 (2018). [PubMed: 30202049]
14. Lei G, Mao C, Yan Y, Zhuang L, and Gan B Ferroptosis, radiotherapy, and combination therapeutic strategies. Protein & cell 12, 836–857 (2021). [PubMed: 33891303]
15. Anandhan A, Dodson M, Shakya A, Chen J, Liu P, Wei Y, Tan H, Wang Q, Jiang Z, and Yang K NRF2 controls iron homeostasis and ferroptosis through HERC2 and VAMP8. Science Advances 9, eade9585 (2023). [PubMed: 36724221]
16. Sun X, Ou Z, Chen R, Niu X, Chen D, Kang R, and Tang D Activation of the p62-Keap1-NRF2 pathway protects against ferroptosis in hepatocellular carcinoma cells. Hepatology 63, 173–184 (2016). [PubMed: 26403645]
17. Koppula P, Lei G, Zhang Y, Yan Y, Mao C, Kondiparthi L, Shi J, Liu X, Horbath A, and Das M A targetable CoQ-FSP1 axis drives ferroptosis-and radiation-resistance in KEAP1 inactive lung cancers. Nature communications 13, 2206 (2022).

18. Dodson M, Castro-Portuguez R, and Zhang DD NRF2 plays a critical role in mitigating lipid peroxidation and ferroptosis. Redox biology 23, 101107 (2019). [PubMed: 30692038]
19. Shakya A, McKee NW, Dodson M, Chapman E, and Zhang DD Anti-Ferroptotic Effects of Nrf2: Beyond the Antioxidant Response. Molecules and Cells 46, 165 (2023). [PubMed: 36994475]
20. Chen D, Tavana O, Chu B, Erber L, Chen Y, Baer R, and Gu W NRF2 is a major target of ARF in p53-independent tumor suppression. Molecular cell 68, 224–232. e224 (2017). [PubMed: 28985506]
21. Wang M-E, Chen J, Lu Y, Bawcom AR, Wu J, Ou J, Asara JM, Armstrong AJ, Wang Q, and Li L RB1-deficient prostate tumor growth and metastasis are vulnerable to ferroptosis induction via the E2F/ACSL4 axis. The Journal of clinical investigation 133 (2023).
22. Liu K, Huang J, Liu J, Klionsky DJ, Kang R, and Tang D Induction of autophagy-dependent ferroptosis to eliminate drug-tolerant human retinoblastoma cells. Cell Death & Disease 13, 521 (2022). [PubMed: 35654783]
23. Chen X, Kang R, Kroemer G, and Tang D Targeting ferroptosis in pancreatic cancer: a double-edged sword. Trends in Cancer 7, 891–901 (2021). [PubMed: 34023326]
24. Yi J, Zhu J, Wu J, Thompson CB, and Jiang X Oncogenic activation of PI3K-AKT-mTOR signaling suppresses ferroptosis via SREBP-mediated lipogenesis. Proceedings of the National Academy of Sciences 117, 31189–31197 (2020).
25. Zhang Y, Swanda RV, Nie L, Liu X, Wang C, Lee H, Lei G, Mao C, Koppula P, and Cheng W mTORC1 couples cyst (e) ine availability with GPX4 protein synthesis and ferroptosis regulation. Nature communications 12, 1589 (2021).
26. Magtanong L, Mueller GD, Williams KJ, Billmann M, Chan K, Armenta DA, Pope LE, Moffat J, Boone C, and Myers CL Context-dependent regulation of ferroptosis sensitivity. Cell chemical biology 29, 1409–1418. e1406 (2022). [PubMed: 35809566]
27. Armenta DA, Laqtom NN, Alchemy G, Dong W, Morrow D, Poltorack CD, Nathanson DA, Abu-Remalieh M, and Dixon SJ Ferroptosis inhibition by lysosome-dependent catabolism of extracellular protein. Cell Chemical Biology 29, 1588–1600. e1587 (2022). [PubMed: 36306785]
28. Du W, Frankel TL, Green M, and Zou W IFNγ signaling integrity in colorectal cancer immunity and immunotherapy. Cellular & molecular immunology 19, 23–32 (2022). [PubMed: 34385592]
29. Wang W, Green M, Choi JE, Gijón M, Kennedy PD, Johnson JK, Liao P, Lang X, Kryczek I, and Sell A CD8+ T cells regulate tumour ferroptosis during cancer immunotherapy. Nature 569, 270–274 (2019). [PubMed: 31043744]
30. Lang X, Green MD, Wang W, Yu J, Choi JE, Jiang L, Liao P, Zhou J, Zhang Q, and Dow A Radiotherapy and Immunotherapy Promote Tumoral Lipid Oxidation and Ferroptosis via Synergistic Repression of SLC7A11Ferroptosis Connects Radiotherapy and Immunotherapy. Cancer discovery 9, 1673–1685 (2019). [PubMed: 31554642]
31. Liao P, Wang W, Wang W, Kryczek I, Li X, Bian Y, Sell A, Wei S, Grove S, and Johnson JK CD8+ T cells and fatty acids orchestrate tumor ferroptosis and immunity via ACSL4. Cancer cell 40, 365–378. e366 (2022). [PubMed: 35216678]
32. Kim R, Hashimoto A, Markosyan N, Tyurin VA, Tyurina YY, Kar G, Fu S, Sehgal M, Garcia-Gerique L, and Kossenkov A Ferroptosis of tumour neutrophils causes immune suppression in cancer. Nature, 1–9 (2022).
33. Wiernicki B, Maschalidi S, Pinney J, Adjemian S, Vanden Berghe T, Ravichandran KS, and Vandenabeele P Cancer cells dying from ferroptosis impede dendritic cell-mediated anti-tumor immunity. Nature communications 13, 3676 (2022).
34. Hayashi K, Nikolos F, Lee Y, Jain A, Tsouko E, Gao H, Kasabyan A, Leung H, Osipov A, and Jung S Tipping the immunostimulatory and inhibitory DAMP balance to harness immunogenic cell death. Nature communications 11, 6299 (2020).
35. Bluml S, Kirchberger S, Bochkov VN, Krönke G, Stuhlmeier K, Majdic O, Zlabinger GJ, Knapp W, Binder BR, and Stöckl J Oxidized phospholipids negatively regulate dendritic cell maturation induced by TLRs and CD40. The Journal of Immunology 175, 501–508 (2005). [PubMed: 15972685]
36. Blüml S, Zupkovitz G, Kirchberger S, Seyerl M, Bochkov VN, Stuhlmeier K, Majdic O, Zlabinger GJ, Seiser C, and Stöckl J Epigenetic regulation of dendritic cell differentiation and function by

oxidized phospholipids. Blood, The Journal of the American Society of Hematology 114, 5481–5489 (2009).

37. Hangai S, Ao T, Kimura Y, Matsuki K, Kawamura T, Negishi H, Nishio J, Kodama T, Taniguchi T, and Yanai H PGE2 induced in and released by dying cells functions as an inhibitory DAMP. Proceedings of the National Academy of Sciences 113, 3844–3849 (2016).
38. Chen D, Chu B, Yang X, Liu Z, Jin Y, Kon N, Rabadan R, Jiang X, Stockwell BR, and Gu W iPLA2β-mediated lipid detoxification controls p53-driven ferroptosis independent of GPX4. Nature Communications 12, 1–15 (2021).
39. Zou Y, Henry WS, Ricq EL, Graham ET, Phadnis VV, Maretich P, Paradkar S, Boehnke N, Deik AA, and Reinhardt F Plasticity of ether lipids promotes ferroptosis susceptibility and evasion. Nature 585, 603–608 (2020). [PubMed: 32939090]
40. Grube J, Woitok MM, Mohs A, Erschfeld S, Lynen C, Trautwein C, and Otto T ACSL4-dependent ferroptosis does not represent a tumor-suppressive mechanism but ACSL4 rather promotes liver cancer progression. Cell Death & Disease 13, 704 (2022). [PubMed: 35963845]
41. Wang X, Li Y, Li Z, Lin S, Wang H, Sun J, Lan C, Wu L, Sun D, and Huang C Mitochondrial calcium uniporter drives metastasis and confers a targetable cystine dependency in pancreatic cancer. Cancer Research 82, 2254–2268 (2022). [PubMed: 35413105]
42. Badgley MA, Kremer DM, Maurer HC, DelGiorno KE, Lee H-J, Purohit V, Sagalovskiy IR, Ma A, Kapilian J, and Firl CE Cysteine depletion induces pancreatic tumor ferroptosis in mice. Science 368, 85–89 (2020). [PubMed: 32241947]
43. Li W, Xu H, Xiao T, Cong L, Love MI, Zhang F, Irizarry RA, Liu JS, Brown M, and Liu XS MAGeCK enables robust identification of essential genes from genome-scale CRISPR/Cas9 knockout screens. Genome biology 15, 1–12 (2014).
44. Salas M, John R, Saxena A, Barton S, Frank D, Fitzpatrick G, Higgins MJ, and Tycko B Placental growth retardation due to loss of imprinting of Phlda2. Mechanisms of development 121, 1199–1210 (2004). [PubMed: 15327781]
45. Frank D, Fortino W, Clark L, Musalo R, Wang W, Saxena A, Li C-M, Reik W, Ludwig T, and Tycko B Placental overgrowth in mice lacking the imprinted gene Ipl. Proceedings of the National Academy of Sciences 99, 7490–7495 (2002).
46. Janssen AB, Tunster SJ, Heazell AE, and John RM Placental PHLDA2 expression is increased in cases of fetal growth restriction following reduced fetal movements. BMC medical genetics 17, 1–5 (2016). [PubMed: 26729329]
47. McMinn J, Wei M, Schupf N, Cusmai J, Johnson E, Smith A, Weksberg R, Thaker H, and Tycko B Unbalanced placental expression of imprinted genes in human intrauterine growth restriction. Placenta 27, 540–549 (2006). [PubMed: 16125225]
48. Schwienbacher C, Angioni A, Scelfo R, Veronese A, Calin GA, Massazza G, Hatada I, Barbanti-Brodano G, and Negrini M Abnormal RNA expression of 11p15 imprinted genes and kidney developmental genes in Wilms' tumor. Cancer Research 60, 1521–1525 (2000). [PubMed: 10749116]
49. Müller S, Van Den Boom D, Zirkel D, Köster H, Berthold F, Schwab M, Westphal M, and Zumkeller W Retention of imprinting of the human apoptosis-related gene TSSC3 in human brain tumors. Human molecular genetics 9, 757–763 (2000). [PubMed: 10749982]
50. Maddika S, Kavela S, Rani N, Palicharla VR, Pokorny JL, Sarkaria JN, and Chen J WWP2 is an E3 ubiquitin ligase for PTEN. Nat Cell Biol 13, 728–733 (2011). [PubMed: 21532586]
51. Wang W, Xiao ZD, Li X, Aziz KE, Gan B, Johnson RL, and Chen J AMPK modulates Hippo pathway activity to regulate energy homeostasis. Nat Cell Biol 17, 490–499 (2015). [PubMed: 25751139]
52. Kagan VE, Mao G, Qu F, Angeli JPF, Doll S, St Croix C, Dar HH, Liu B, Tyurin VA, and Ritov VB Oxidized arachidonic and adrenic PEs navigate cells to ferroptosis. Nature chemical biology 13, 81–90 (2017). [PubMed: 27842066]
53. Tyurina YY, Kapralov AA, Tyurin VA, Shurin G, Amoscato AA, Rajasundaram D, Tian H, Bunimovich YL, Nefedova Y, and Herrick WG Redox phospholipidomics discovers pro-ferroptotic death signals in A375 melanoma cells in vitro and in vivo. Redox Biology 61, 102650 (2023). [PubMed: 36870109]

54. Wiernicki B, Dubois H, Tyurina YY, Hassannia B, Bayir H, Kagan VE, Vandenabeele P, Wullaert A, and Vanden Berghe T Excessive phospholipid peroxidation distinguishes ferroptosis from other cell death modes including pyroptosis. Cell death & disease 11, 922 (2020). [PubMed: 33110056]
55. Beatty A, Singh T, Tyurina YY, Tyurin VA, Samovich S, Nicolas E, Maslar K, Zhou Y, Cai KQ, and Tan Y Ferroptotic cell death triggered by conjugated linolenic acids is mediated by ACSL1. Nature Communications 12, 2244 (2021).
56. Singh NK, and Rao GN Emerging role of 12/15-Lipoxygenase (ALOX15) in human pathologies. Progress in lipid research 73, 28–45 (2019). [PubMed: 30472260]
57. Saxena A, Morozov P, Frank D, Musalo R, Lemmon MA, Skolnik EY, and Tycko B Phosphoinositide binding by the pleckstrin homology domains of Ipl and Tih1. Journal of Biological Chemistry 277, 49935–49944 (2002). [PubMed: 12374806]
58. Agarwal AK, Sukumaran S, Bartz R, Barnes RI, and Garg A Functional characterization of human 1-acylglycerol-3-phosphate-O-acyltransferase isoform 9: cloning, tissue distribution, gene structure, and enzymatic activity. Journal of endocrinology 193, 445–457 (2007). [PubMed: 17535882]
59. Sukumaran S, Barnes RI, Garg A, and Agarwal AK Functional characterization of the human 1-acylglycerol-3-phosphate-O-acyltransferase isoform 10/glycerol-3-phosphate acyltransferase isoform 3. Journal of molecular endocrinology 42, 469–478 (2009). [PubMed: 19318427]
60. Valentine WJ, Yanagida K, Kawana H, Kono N, Noda NN, Aoki J, and Shindou H Update and nomenclature proposal for mammalian lysophospholipid acyltransferases, which create membrane phospholipid diversity. Journal of Biological Chemistry 298 (2022).
61. Hanahan D, and Weinberg RA Hallmarks of cancer: the next generation. cell 144, 646–674 (2011). [PubMed: 21376230]
62. Schafer ZT, Grassian AR, Song L, Jiang Z, Gerhart-Hines Z, Irie HY, Gao S, Puigserver P, and Brugge JS Antioxidant and oncogene rescue of metabolic defects caused by loss of matrix attachment. Nature 461, 109–113 (2009). [PubMed: 19693011]
63. Jiang L, Shestov AA, Swain P, Yang C, Parker SJ, Wang QA, Terada LS, Adams ND, McCabe MT, and Pietrak B Reductive carboxylation supports redox homeostasis during anchorage-independent growth. Nature 532, 255–258 (2016). [PubMed: 27049945]
64. Labuschagne CF, Cheung EC, Blagih J, Domart M-C, and Vousden KH Cell clustering promotes a metabolic switch that supports metastatic colonization. Cell metabolism 30, 720–734. e725 (2019). [PubMed: 31447323]
65. Eischen CM, Weber JD, Roussel MF, Sherr CJ, and Cleveland JL Disruption of the ARF–Mdm2–p53 tumor suppressor pathway in Myc-induced lymphomagenesis. Genes & development 13, 2658–2669 (1999). [PubMed: 10541552]
66. Yang WS, SriRamaratnam R, Welsch ME, Shimada K, Skouta R, Viswanathan VS, Cheah JH, Clemons PA, Shamji AF, and Clish CB Regulation of ferroptotic cancer cell death by GPX4. Cell 156, 317–331 (2014). [PubMed: 24439385]
67. Matsushita M, Freigang S, Schneider C, Conrad M, Bornkamm GW, and Kopf M T cell lipid peroxidation induces ferroptosis and prevents immunity to infection. Journal of Experimental Medicine 212, 555–568 (2015). [PubMed: 25824823]
68. Doll S, Proneth B, Tyurina YY, Panzilius E, Kobayashi S, Ingold I, Irmler M, Beckers J, Aichler M, and Walch A ACSL4 dictates ferroptosis sensitivity by shaping cellular lipid composition. Nature chemical biology 13, 91–98 (2017). [PubMed: 27842070]
69. Yoo S-E, Chen L, Na R, Liu Y, Rios C, Van Remmen H, Richardson A, and Ran Q Gpx4 ablation in adult mice results in a lethal phenotype accompanied by neuronal loss in brain. Free Radical Biology and Medicine 52, 1820–1827 (2012). [PubMed: 22401858]
70. Informatics MG Obtaining and Loading Phenotype Annotations from the International Mouse Phenotyping Consortium (IMPC) Database. Database Release (2014).
71. Memon A, Pyao Y, Jung Y, Lee JI, and Lee WK A modified protocol of diethylnitrosamine administration in mice to model hepatocellular carcinoma. International journal of molecular sciences 21, 5461 (2020). [PubMed: 32751728]

72. Concordet J-P, and Haeussler M CRISPOR: intuitive guide selection for CRISPR/Cas9 genome editing experiments and screens. Nucleic acids research 46, W242–W245 (2018). [PubMed: 29762716]

73. Dove SK, and Michell RH Inositol lipid-dependent functions in Saccharomyces cerevisiae: analysis of phosphatidylinositol phosphates. Lipid Signaling Protocols, 1–16 (2009).

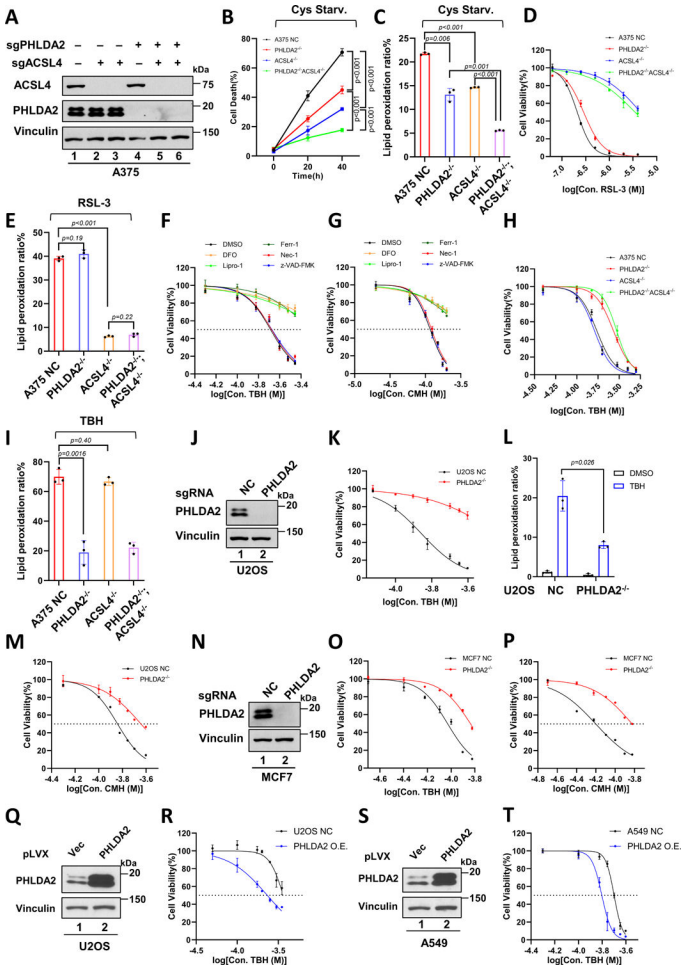

Figure 1. Identification of PHLDA2 as a critical factor for ferroptosis induced by cystine starvation independent of GPX4 inhibition

(**A**) Western blot analysis of A375 cells expressing sgNC (negative control), sgPHLDA2, sgACSL4, or sgPHLDA2/ACSL4 (referred to as NC, PHLDA2$^{-/-}$, ACSL4$^{-/-}$, or PHLDA2$^{-/-}$;ACSL4$^{-/-}$ A375 cells).

(**B**)Time-dependent of cystine deprivation induced cell death of Negative control (NC), PHLDA2$^{-/-}$, ACSL4$^{-/-}$, or PHLDA2$^{-/-}$;ACSL4$^{-/-}$A375 cells.

(**C**) Lipid peroxidation ratio of NC, PHLDA2$^{-/-}$, ACSL4$^{-/-}$, or PHLDA2$^{-/-}$;ACSL4$^{-/-}$A375 cells cultured in cystine deprived medium for 18h.

(**D**) Cell viability of NC, PHLDA2$^{-/-}$, ACSL4$^{-/-}$, or PHLDA2$^{-/-}$;ACSL4$^{-/-}$A375 cells treated with RSL-3 for 8h.

(**E**) Lipid peroxidation ratio of NC, PHLDA2$^{-/-}$, ACSL4$^{-/-}$, or PHLDA2$^{-/-}$;ACSL4$^{-/-}$A375 cells under RSL-3 (500nM) treatment for 4h.

(**F**) Cell viability of A375 cells treated with TBH in the presence of DMSO, DFO (50μM), liproxstatin-1 (Lipro-1, 5μM), ferrostatin-1 (Ferr-1, 5μM), necrostatin-1 (Nec-1, 10μM), or z-VAD-FMK (20μM) for 8h.

(**G**) Cell viability of A375 cells treated with CMH in the presence of DMSO, DFO (50μM), liproxstatin-1 (5μM), ferrostatin-1 (5μM), necrostatin-1 (10μM), or z-VAD-FMK (20μM) for 6h.

(**H**) Cell viability of NC, PHLDA2$^{-/-}$, ACSL4$^{-/-}$, or PHLDA2$^{-/-}$;ACSL4$^{-/-}$A375 cells treated under TBH treatment for 6h.
(**I**) Lipid peroxidation ratio of NC, PHLDA2$^{-/-}$, ACSL4$^{-/-}$, or PHLDA2$^{-/-}$;ACSL4$^{-/-}$A375 cells under TBH (200μM) treatment for 3h.
(**J**) Western blot analysis of U2OS cells expressing sgPHLDA2 (referred to as PHLDA2$^{-/-}$ U2OS cells).
(**K**) Cell viability of NC or PHLDA2$^{-/-}$ U2OS cells treated with TBH for 8h.
(**L**) Lipid peroxidation ratio of NC or PHLDA2$^{-/-}$ U2OS cells treated with TBH for 4h.
(**M**) Cell viability of NC or PHLDA2$^{-/-}$ U2OS cells treated with CMH for 6h.
(**N**) Western blot analysis of MCF7 cells expressing sgPHLDA2 (referred to as PHLDA2$^{-/-}$ MCF7 cells).
(**O**) Cell viability of NC or PHLDA2$^{-/-}$ MCF7 cells treated with TBH for 8h.
(**P**) Cell viability of NC or PHLDA2$^{-/-}$ MCF7 cells treated with CMH for 8h.
(**Q**) Western blot analysis of U2OS cells stably expressing empty vector (Vec) or PHLDA2.
(**R**) Cell viability of U2OS Vec or PHLDA2-overexpressing cells TBH for 8h.
(**S**) Western blot analysis of A549 cells stably expressing empty vector (Vec) or PHLDA2.
(**T**)Cell viability of A549 Vec or PHLDA2-overexpressing cells TBH for 8h.
Data are the mean ± SD of n = 3 biological repeats. *p* values were calculated using unpaired, two-tailed Student's *t*-test.

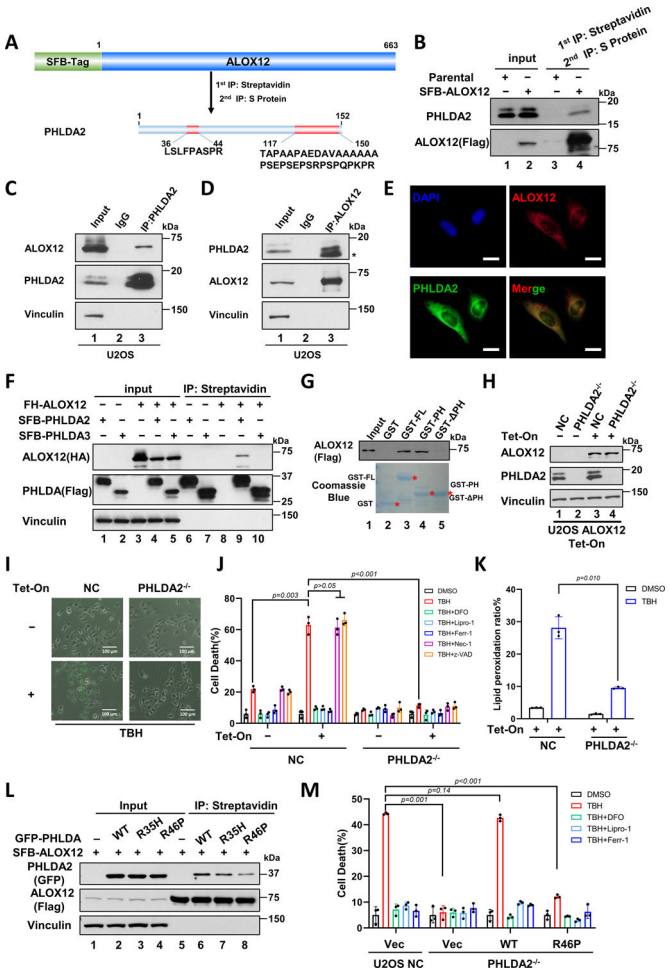

Figure 2. PHLDA2 plays an important role in modulating ROS-induced ferroptosis by interacting the ALOX12 lipoxygenase

(**A**) Schematic diagram of the SFB-tagged ALOX12. PHLDA2 peptides identified from ALOX12 associated complexed by liquid chromatography mass spectrometry/mass spectrometry (LC–MS/MS) are shown. A total of 2 unique PHLDA2 peptides have 28.29% coverage of the whole PHLDA2 protein. SFB, triple S protein, Flag, and Streptavidin binding peptide.

(**B**) Western blot of affinity-purified protein complexes from SFB-ALOX12 stable H1299 cells or the parental H1299 cells.

(**C** and **D**) Western blot analysis of endogenous interaction between ALOX12 and PHLDA2 in U2OS cells. * : non-specific band.

(**E**) U2OS cells were fixed and immune-stained with anti-ALOX12 antibody (red) or anti-PHLDA2 antibody (green). DAPI (blue) represents nucleus. Scale bar, 25 μm.

(**F**) Western blot analysis of the interaction between overexpressed ALOX12 and/or PHLDA2, PHLDA3 in H1299 cells. IP, immunoprecipitation. FH, double epitope Flag and HA tag.

(**G**) *In vitro* binding assay of GST fused PHLDA2 FL, PH, ΔPH and purified ALOX12. PHLDA2-FL, amino acids 1–152; PHLDA2-PH, amino acids 7–101; PHLDA2-ΔPH, amino acids 102–152.

(**H**) Western blot analysis of NC or PHLDA2$^{-/-}$ ALOX12 Tet-on U2OS cells pre-incubated with doxycycline (0.5μg/mL; Tet-On) for 24h.
(**I**) Representative phase-contrast SYTOX stained images of NC or PHLDA2$^{-/-}$ ALOX12 Tet-on U2OS cells pre-incubated with doxycycline (0.5μg/mL; Tet-On) for 24h then treated with TBH (300 μM) for 6h. Scale bars, 100 μm.
(**J**) Cell death of NC or PHLDA2$^{-/-}$ ALOX12 Tet-on U2OS cells pre-incubated with doxycycline (0.5μg/mL; Tet-On) for 24h then treated with TBH (300μM) for 8h.
(**K**) Lipid peroxidation ratio of NC or PHLDA2$^{-/-}$ ALOX12 Tet-on U2OS cells pre-incubated with doxycycline (0.5μg/mL; Tet-On) for 24h then treated with TBH (300μM) for 4h.
(**L**) Western blot analysis of the interaction between overexpressed ALOX12 and/or PHLDA2 cancer hotspot mutant R35H, R46P in H1299 cells.
(**M**) Cell death of PHLDA2$^{-/-}$ U2OS cells ectopically expressing Vector, GFP tagged PHLDA2 WT or R46P under TBH treatment for 8h.
Data are the mean ± SD of n = 3 biological repeats. *p* values were calculated using unpaired, two-tailed Student's *t*-test.

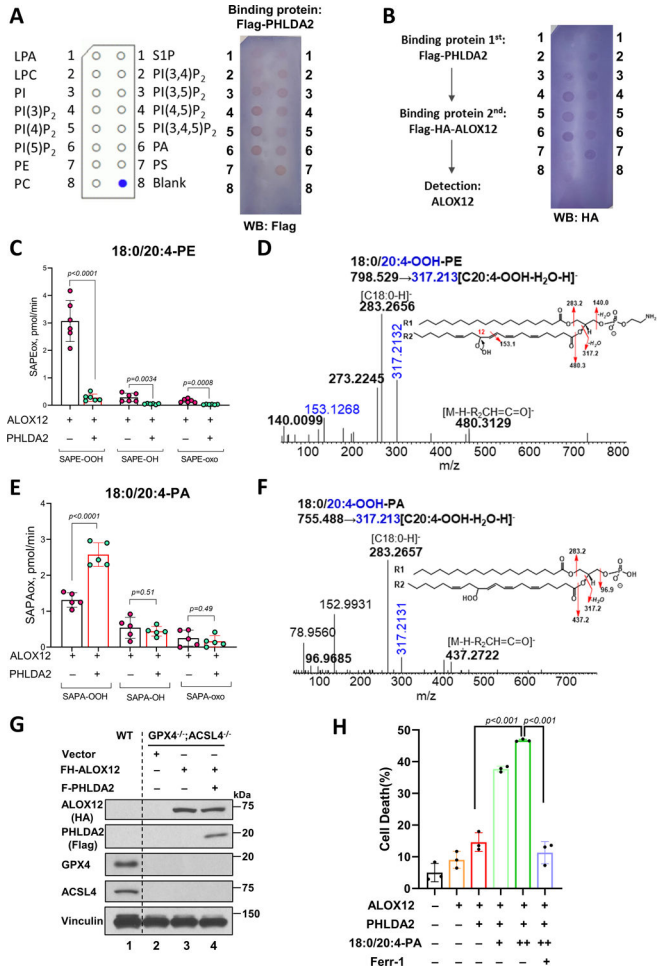

Figure 3. PHLDA2 preferentially binds phosphatidic acid (PA) for phospholipid peroxidation

(**A**) Binding of PHLDA2 to PIP Strips. The spots annotation and relative localization were shown in numbers. Bound PHLDA2 proteins were detected with K-TMBP substrate.

(**B**) Binding of ALOX12 to PIP Strips through PHLDA2. Left: Workflow of ALOX12 binding to PIP Strips by interacting PHLDA2. Right: The spots annotation and relative localization were shown in numbers. Bound ALOX12 proteins were detected with K-TMBP substrate.

(**C**) Oxidation of phospholipids by ALOX12 or ALOX12/PHLDA2 complex in DOPC liposomes. Stearoyl-arachidonoyl-Phosphatidylethanolamine (SAPE, 18:0/20:4-PE).

(**D**) Fragmentation analysis shows typical MS2 spectra of 18:0/20:4-OOH-PE (m/z 798.5291) accumulated during oxidation of corresponding phospholipids by ALOX12 or ALOX12/PHLDA2 complex in DOPC liposomes. Fragmentation patterns of molecular ion with m/z 317.213 corresponds to 20:4-OOH minus water. The fragment with m/z 153.126 is diagnostic for the OOH-groups at position C12 *sn2*-20:4 of the fatty acyl chain. Inserts: displays structural analysis of phospholipids, where arrows show typical MS/MS fragments.

(**E**) Oxidation of phospholipids by ALOX12 or ALOX12/PHLDA2 complex in DOPC liposomes. Stearoyl-arachidonoyl-Phosphatidic acid (SAPA, 18:0/20:4-PA).

(**F**) Fragmentation analysis shows typical MS2 spectra of 18:0/20:4-OOH-PA (m/z 755.4882) accumulated during oxidation of corresponding phospholipids by ALOX12 or ALOX12/PHLDA2 complex in DOPC liposomes. Fragmentation patterns of molecular ion with m/z 317.213 corresponds to 20:4-OOH minus water. The fragment with m/z 153.126 is diagnostic for the OOH-groups at position C12 *sn2*-20:4 of the fatty acyl chain. Inserts: displays structural analysis of phospholipids, where arrows show typical MS/MS fragments.
(**G**) Western blot analysis of ACSL4$^{-/-}$;GPX4$^{-/-}$ A375 cells ectopically expressing Vector, ALOX12 and/or PHLDA2. WT cells were used as control.
(**H**) Cell death ratio of ACSL4$^{-/-}$;GPX4$^{-/-}$ A375 cells ectopically expressing Vector, ALOX12 and/or PHLDA2 under SAPA: DOPC liposome (25μM or 50μM) incubation with or without Ferr-1 (5μM) for 24h.
Data are the mean ± SD of n = 6 (**C**), n=5 (**E**) or n=3 (**H**) biological repeats. *p* values were calculated using unpaired, two-tailed Student's *t*-test.

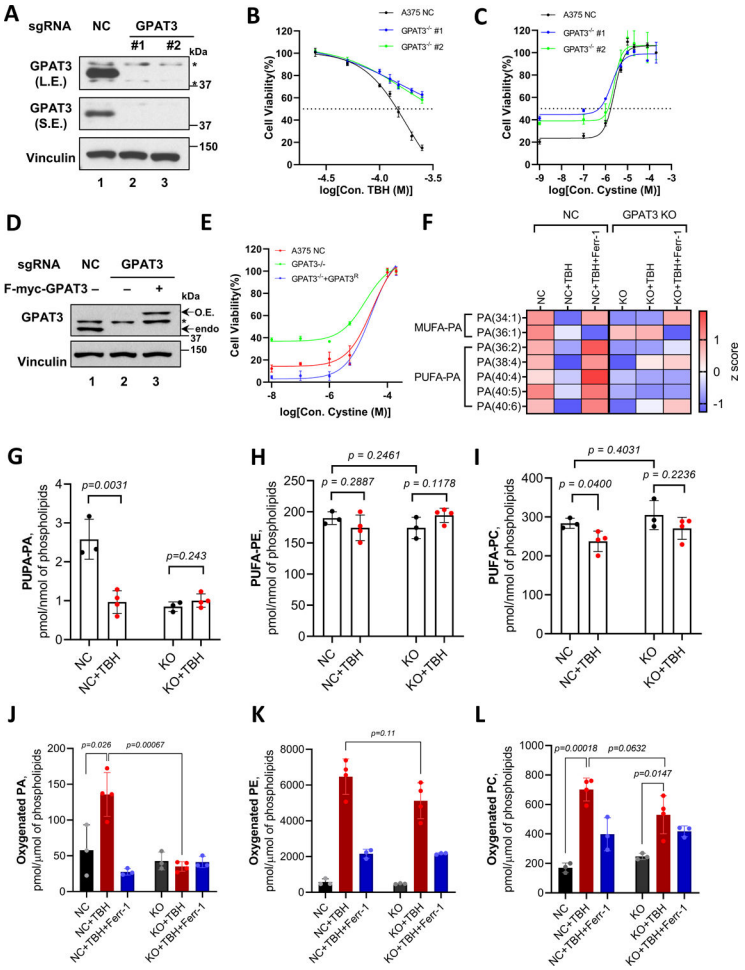

Figure 4. Oxidation of phosphatidic acid (PA), but not phosphatidylethanolamine (PE) is critical for ROS-induced ferroptosis

(**A**) Western blot analysis of NC, sgGPAT3 #1, or sgGPAT3 #2 A375 cells (referred to as GPAT3$^{-/-}$ #1 or GPAT3$^{-/-}$ #2). * : non-specific band.

(**B**) Cell viability of NC, GPAT3$^{-/-}$ #1, or GPAT3$^{-/-}$ #2 A375 cells treated with TBH for 8h.

(**C**) Cell viability of NC, GPAT3$^{-/-}$ #1, or GPAT3$^{-/-}$ #2 A375 cells under cystine starvation for 24h.

(**D**) Western blot analysis of NC, GPAT3$^{-/-}$ #1, or GPAT3$^{-/-}$ #2 re-expressed GPAT3 A375 cells. Arrows indicate the band of overexpression of GPAT3 (referred to as O.E.) and endogenous of GPAT3 (referred to as endo). * : non-specific band.

(**E**) Cell viability of NC, GPAT3$^{-/-}$ #1, or GPAT3$^{-/-}$ #2 re-expressed GPAT3 A375 cells under cystine starvation for 24h.

(**F**) Changes in PA content. Data are presented as heat map, autoscaled to z scores, and coded blue (low values) to red (high values). Note: A marked change was observed for the contents of PA esterified PUFA molecular species in WT A375 cells after treatment with TBH. In the presence of Ferr-1, the contents of PUFA-PA species remained unchanged in WT cells.

(**G-I**) Total content of PUFA-PA molecular species (**G**), PUFA-PE (di-acyl and plasmalogen) molecular species (**H**), and PUFA-PC (di-acyl and plasmalogen) molecular

species (**I**) in WT or GPAT3 KO A375 cells treated with or without TBH. The data show a significant difference in consumption of PUFA-PA for WT after TBH treatment. Peroxidation of PUFAs-PA leads to decrease of phospholipids content in WT A375 cells. (**J**-**L**) Total content of oxygenated PA (**J**), PE (**K**), and PC (**L**) in WT or GPAT3 KO A375 cells exposed to TBH with or without Ferr-1.

For **B**, **C**, and **E**, data are the mean ± SD of n = 3 biological repeats. For **F**-**L**, three biological repeats were measured from NC or GPAT3 KO A375 cells without treatment or with TBH plus Ferr-1 treatment, and four biological repeats were measured from NC or GPAT3 KO A375 cells with TBH treatment. *p* values were calculated using unpaired, two-tailed Student's *t*-test.

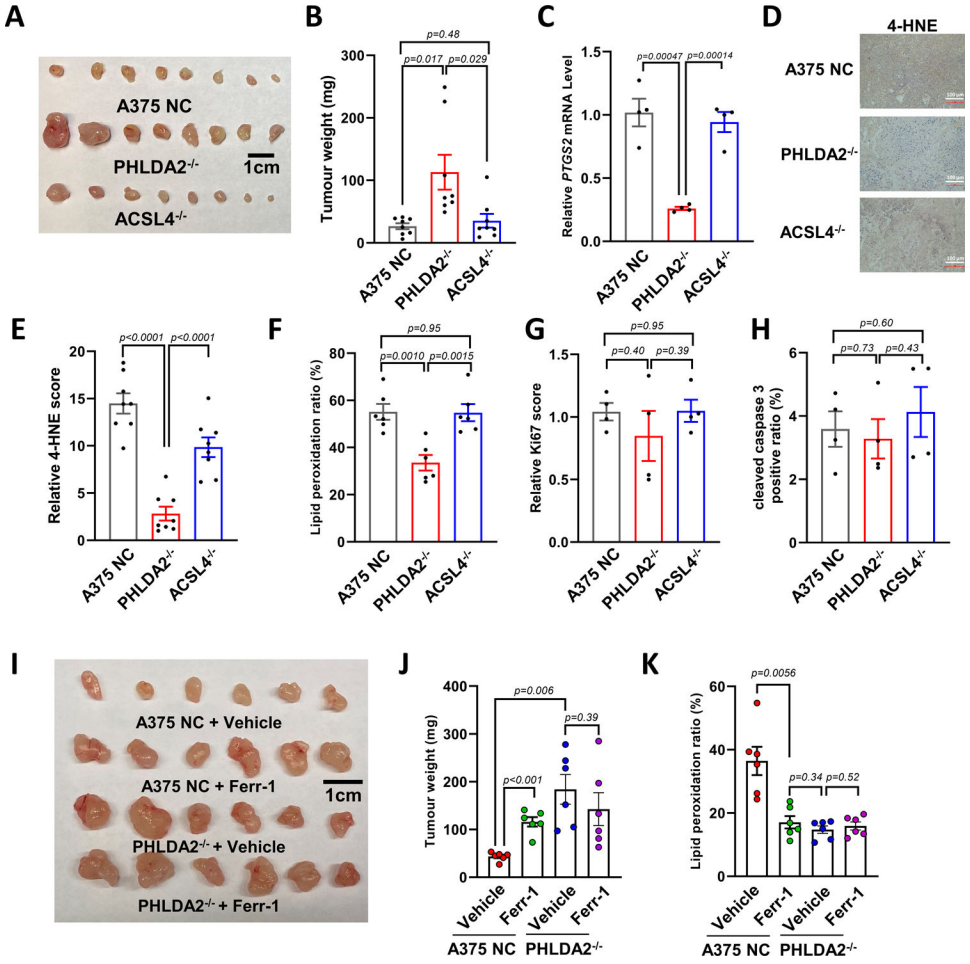

Figure 5. PHLDA2-mediated ferroptosis is required for tumor suppression in immunodeficient mouse models.

(**A**) Xenograft tumors of NC, PHLDA2$^{-/-}$, or ACSL4$^{-/-}$ A375 cells in *Nu/Nu* mice. n = 8 independent tumors per group. Scale bars, 1cm.

(**B**) Tumor weights from tumors harvested in (**A**).

(**C**) RT-qPCR of *PTGS2* mRNA from tumors harvested in (**A**).

(**D**) Representative images of immunochemistry 4-HNE staining of the tissues from tumors harvested in (**A**). 20X, scale bars, 100μm.

(**E**) Immunochemistry 4-HNE score from tumors harvested in (**A**).

(**F**) Lipid peroxidation ratio of tumor derived cells from (**A**).

(**G**) Quantification of cleaved caspase 3 positive ratio from (**A**).

(**H**) Levels of relative Ki67 score from (**A**).

(**I**) Xenograft tumors of A375 NC or PHLDA2$^{-/-}$ cells in *Nu/Nu* mice without or with 1mg/kg Ferr-1 treatment. n = 6 independent tumors per group. Scale bars, 1cm.

(**J**) Tumor weights from tumors harvested in (**I**).

(**K**) Lipid peroxidation ratio of tumor derived cells from (**I**).

For **B** and **J**, data are mean ± SEM. of n = 8 (**B**) or n = 6 (**J**) tumors. Data are the mean ± SD of n = 8 (**E**), n=6 (**F** and **K**), or n = 4 (**C**, **G**, and **H**) biological repeats. *p* values were calculated using unpaired, two-tailed Student's *t*-test.

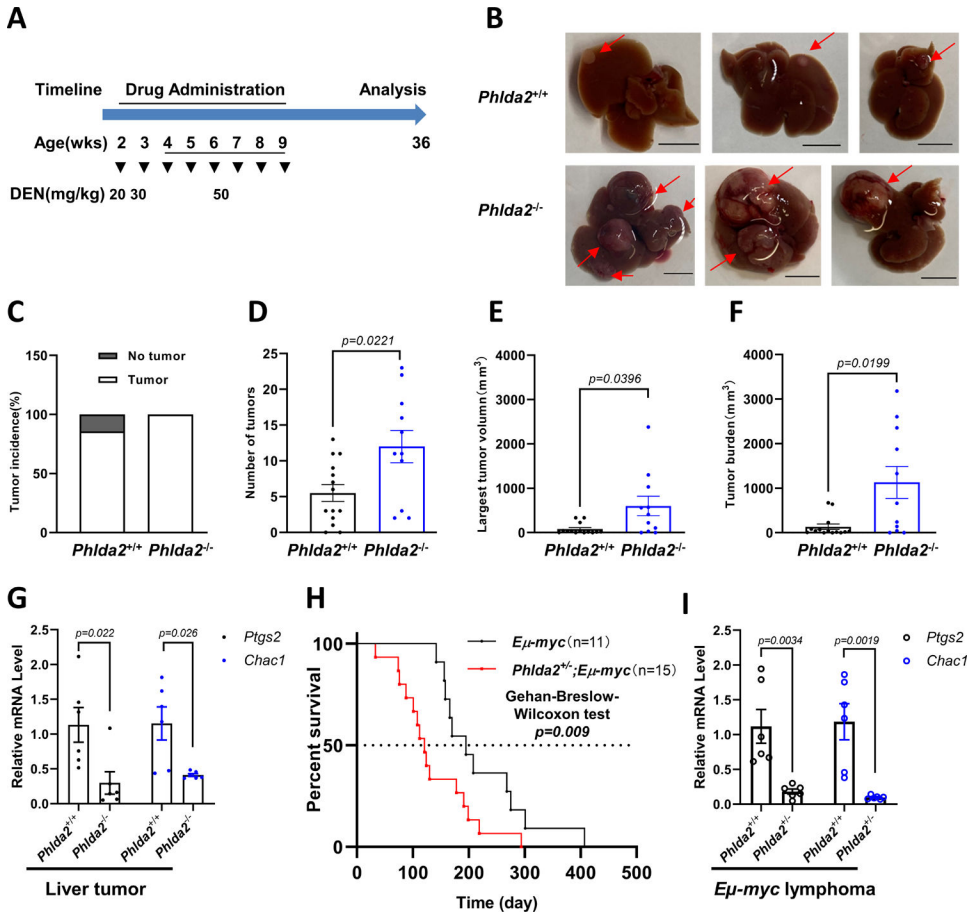

Figure 6. PHLDA2-mediated ferroptosis is crucial for tumor suppression in the immunocompetent mice

(**A**) Scheme of the DEN induced HCC mouse model. DEN administration started from 2-week-old mice with indicated dosage. After 8-week DEN administration, mice were grown for additional 27 weeks before analysis.

(**B**) Representative liver pictures from DEN-treated *Phlda2*$^{+/+}$ and *Phlda2*$^{-/-}$ mice. Arrows indicate the locations of tumors. Scale bars, 1cm.

(**C**-**F**) Tumor incidence (**C**), the total number of liver tumors (**D**), the largest tumor volume (**E**), and the total tumor burden (**F**) determined from *Phlda2*$^{+/+}$ (n = 14) and *Phlda2*$^{-/-}$ (n = 11) mice. *p* values were calculated using unpaired, two-tailed Student's *t*-test.

(**G**) RT-qPCR of mouse *Ptgs2* and *Chac1* mRNA from liver tumors harvested from *Phlda2*$^{+/+}$ or *Phlda2*$^{-/-}$ mice. Data are the mean ± SEM of n = 6 tumors. *p* values were calculated using unpaired, two-tailed Student's *t*-test.

(**H**) Kaplan-Meier survival curves of *Eμ-Myc* (n = 11) or *Phlda2*$^{-/-}$; *Eμ-Myc* (n = 15) mice. *p* value was calculated using Gehan-Breslow-Wilcoxon test.

(**I**) RT-qPCR of mouse *Ptgs2* and *Chac1* mRNA of tumors from *Eμ-Myc* mice and from *Phlda2*$^{-/-}$;*Eμ-Myc* mice. Data are the mean ± SEM of n = 6 tumors. *p* values were calculated using unpaired, two-tailed Student's *t*-test.

Key resources table

REAGENT or RESOURCE	SOURCE	IDENTIFIER
Antibodies		
Anti-GFP	Takara Bio	Cat# 632381; RRID: AB_2313808
Anti-PHLDA2	Thermo Fisher Scientific	Cat# PA5-92845; RRID: AB_2806513
Anti-PHLDA2	Proteintech	Cat# 14661-1-AP; RRID: AB_2163294
Anti-GPAT3	Proteintech	Cat# 20603-1-AP; RRID: AB_10694289
Anti-Vinculin	Sigma-Aldrich	Cat# V9131; RRID: AB_477629
Anti-Flag	Sigma-Aldrich	Cat# F-3165; RRID: AB_259529
Anti-Actin	Sigma-Aldrich	Cat# A3853; RRID: AB_262137
Anti-p53 (CM5)	Leica Biosystems	Cat#NCL-L-p53-CM5p; RRID: AB_2895247
Anti-ALOX12	Santa Cruz Biotechnology	Cat# sc-365194; RRID: AB_10709144
Anti-ACSL4	Santa Cruz Biotechnology	Cat# sc-271800; RRID: AB_10715092
Anti-MDM2	Millipore	Cat# OP-145; RRID: AB_2235250
Anti-Hdmx/MDM4	Bethyl	Cat# A300-287A; RRID: AB_263407
Anti-CDKN2A/p19ARF	Abcam	Cat# ab-26696; RRID: AB_776947
Anti-GPX4	Abcam	Cat# ab125066; RRID: AB_10973901
Anti-4-Hydroxynonenal (4-HNE)	Abcam	Cat#ab46545; RRID: AB_722490
Anti-Ki67	Abcam	Cat#ab15580; RRID: AB_443209
Anti-HA	Roche	Cat# 11867423001; RRID: AB_823586
Anti-Cleaved Caspase-3 (Asp175)	Cell Signaling Technology	Cat# 9661; RRID: AB_2341188
Anti-RIP	Cell Signaling Technology	Cat# 3493; RRID: AB_2305314
Anti-Phospho-RIP (Ser166)	Cell Signaling Technology	Cat# 65746; RRID: AB_2799693
Alexa Fluor 488 goat anti-rabbit secondary antibodies	Thermo Fisher Scientific	Cat# A11008; RRID: AB_143165
Alexa Fluor 568 goat anti-mouse secondary antibodies	Thermo Fisher Scientific	Cat# A11004; RRID: AB_2534072
Bacterial and Virus Strains		
DH5α Competent Cells	Thermo Fisher Scientific	18265017
TOP10 Competent Cells	Thermo Fisher Scientific	C404006
ElectroMAX™ Stbl4™ Competent Cells	Thermo Fisher Scientific	11635018
Chemicals, Peptides, and Recombinant Proteins		
Tert-butyl hydroperoxide (TBH)	Sigma-Aldrich	458139; CAS: 75-91-2
Cumene hydroperoxide (CMH)	Sigma-Aldrich	247502; CAS: 80-15-9
1S,3R-RSL-3	Sigma-Aldrich	SML2234; CAS:1219810-16-8
N-acetyl-L-cysteine (NAC)	Sigma-Aldrich	A7250; CAS: 616-91-1
Necrostatin-1 (Nec-1)	Sigma-Aldrich	N9037; CAS: 4311-88-0
Ferrostatin-1 (Ferr-1)	Selleck Chemicals	S7243; CAS: 347174-05-4
Liproxstatin-1 (Lipro-1)	Sigma-Aldrich	SML1414; CAS: 950455-15-9
Deferoxamine (DFO)	Sigma-Aldrich	D9533; CAS: 138-14-7
z-VAD-FMK	Sigma-Aldrich	V116; CAS: 187389-52-2

REAGENT or RESOURCE	SOURCE	IDENTIFIER
Staurosporine	MedChemExpress	HY-15141; CAS: 62996-74-1
N-Nitrosodiethylamine (Diethylnitrosamine, DEN)	Sigma-Aldrich	N0756; CAS: 55-18-5
Glutamine	Sigma-Aldrich	G8540; CAS: 56-85-9
Methionine	Sigma-Aldrich	M5308; CAS: 63-68-3
Cystine	Sigma-Aldrich	C7602; CAS: 56-89-3
18:1/18:1-PC (DOPC)	Avanti Polar Lipids	850375; CAS:4235-95-4
18:0/20:4-PA	Avanti Polar Lipids	840863; CAS: 322647-61-0
18:0/20:4-PE	Avanti Polar Lipids	850804; CAS: 61216-62-4
18:0/20:4-PC	Avanti Polar Lipids	850469; CAS: 35418-59-8
18:0/20:4-PI	Avanti Polar Lipids	850144; CAS: 1331751-28-0
18:0/20:4-PS	Avanti Polar Lipids	840064; CAS: 474967-15-2
18:0/20:4-PI(3)P	Avanti Polar Lipids	850189; CAS: 2315262-42-9
18:0/20:4-PI(3,4)P	Avanti Polar Lipids	850188; CAS: 2315262-41-8
16:0/16:0-PA	Avanti Polar Lipids	830855; CAS: 169051-60-9
Arachidonic acid (C20:4, AA)	Cayman Chemical	90010; CAS: 506-32-1
BODIPY 581/591 C11 dye	Thermo Fisher Scientific	D3861; CAS: 217075-36-0
SYTOX green dead cell stain	Thermo Fisher Scientific	S34860; CAS: 2383063-37-2
Anti-Flag agarose beads	Sigma-Aldrich	A2220
Anti-HA agarose beads	Sigma-Aldrich	A2095
Anti-Streptavidin agarose beads	Sigma-Aldrich	16-126
Flag-peptide	Sigma-Aldrich	F3290
Lipofectamine 3000	Thermo Fisher Scientific	L3000150
Lipofectamine CRISPRMAX Cas9	Thermo Fisher Scientific	CMAX00015
TrueCut Cas9 Protein v2	Thermo Fisher Scientific	A36498
Critical Commercial Assays		
CellTiter-Glo 2.0 Cell Viability Assay	Promega	G9243
CytoTox-ONE Homogeneous Membrane Integrity Assay kit	Promega	G7890
Deposited data		
Raw data	This paper	Mendeley data DOI: 10.17632/6rjv2vwntc.1
Experimental models: Cell lines		
Human: HEK293T	ATCC	CRL-3216
Human: A375	ATCC	CRL-1619
Human: MCF-7	ATCC	HTB-22
Human: A549	ATCC	CCL-185
Human: U2OS	ATCC	HTB-96
Human: H1299	ATCC	CRL-5803
A375 PHLDA2 KO	This paper	N/A
A375 ACSL4 KO	This paper	N/A
A375 GPX4 KO	This paper	N/A

REAGENT or RESOURCE	SOURCE	IDENTIFIER
A375 PHLDA2/ACSL4 double KO	This paper	N/A
A375 GPX4/PHLDA2 double KO	This paper	N/A
A375 GPX4/ACSL4 double KO	This paper	N/A
A375 GPX4/ACSL4/PHLDA2 triple KO	This paper	N/A
A375 PHLDA2 overexpressed	This paper	N/A
U2OS PHLDA2 KO	This paper	N/A
U2OS PHLDA2 overexpressed	This paper	N/A
U2OS ALOX12 Tet-on	This paper	N/A
UOS PHLDA2 KO+ALOX12 Tet-on	This paper	N/A
A549 PHLDA2 overexpressed	This paper	N/A
A549 PHLDA2 KO	This paper	N/A
A549 ACSL4 KO	This paper	N/A
MCF7 PHLDA2 KO	This paper	N/A
Experimental models: Mouse Strains		
C57BL/6 mouse	Charles River	000664
NU/NU nude mouse	Charles River	088
Phlda2 homozygous mouse	Benjamin Tycko	Frank et al., 2002[44]
Eμ-myc mouse	Jackson Laboratory	002728
Oligonucleotides		
Negative Control non-targeting sgRNA	Thermo Fisher Scientific	A35526
PHLDA2 sgRNA #1	Thermo Fisher Scientific	CRISPR676994_SGM
PHLDA2 sgRNA #2	Thermo Fisher Scientific	CRISPR676991_SGM
ACSL4 sgRNA #1	Thermo Fisher Scientific	CRISPR706125_SGM
ACSL4 sgRNA #2	Thermo Fisher Scientific	CRISPR706152_SGM
GPX4 sgRNA	Thermo Fisher Scientific	CRISPR662855_SGM;
GPAT3 sgRNA #1	Thermo Fisher Scientific	CRISPR611043_SGM
GPAT3 sgRNA #2	Thermo Fisher Scientific	CRISPR611046_SGM
AGPAT3 sgRNA #1: 5’ - CCGCCACCTCCATGCTAACG −3’	Synthego	N/A
AGPAT3 sgRNA #2: 5’ - CTCTACGGGAAGAAGTACG −3’	Synthego	N/A
Human *PTGS2* Forward 5’- CTTCACGCATCAGTTTTTCAAG −3’	Sigma-Aldrich	N/A
Human *PTGS2* Reverse 5’- TCACCGTAAATATGATTTAAGTCCAC −3’	Sigma-Aldrich	N/A
Human *GAPDH* Forward 5’- GAAGGTGAAGGTCGGAGTC −3’	Sigma-Aldrich	N/A
Human *GAPDH* Reverse 5’- GAAGATGGTGATGGGATTTC −3’	Sigma-Aldrich	N/A
Mouse *Ptgs2* Forward 5’- CAACTCCCATGGGTGTGAA −3’	Sigma-Aldrich	N/A
Mouse *Ptgs2* Reverse 5’- GTCTGTCCAGAGTTTCACC −3’	Sigma-Aldrich	N/A

REAGENT or RESOURCE	SOURCE	IDENTIFIER
Mouse *Chac1* Forward 5'- GGCTTCGTTCGTGGCTATAG −3'	Sigma-Aldrich	N/A
Mouse *Chac1* Reverse 5'- GCTTCCCTCACATTCAGGT −3'	Sigma-Aldrich	N/A
Mouse *Actin* Forward 5'- GGCTGTATTCCCCTCCATCG −3'	Sigma-Aldrich	N/A
Mouse *Actin* Reverse 5'- CCAGTTGGTAACAATGCCATGT −3'	Sigma-Aldrich	N/A
Recombinant DNA		
pLVX-M-puro-PHLDA2	This paper	N/A
pCIN4-Flag-HA-ALOX12	This paper	N/A
SFB-ALOX12	This paper	N/A
RK5-Flag-PHLDA2	This paper	N/A
GFP-PHLDA1/TDAG51	Addgene	32699
SFB-PHLDA2	This paper	N/A
SFB-PHLDA2 PH	This paper	N/A
SFB-PHLDA2 ΔPH	This paper	N/A
SFB-PHLDA3	This paper	N/A
GFP-PHDLA2	This paper	N/A
GFP-PHLDA2 R35H	This paper	N/A
GFP-PHLDA2 R46P	This paper	N/A
GFP-PHDLA2 BS	This paper	N/A
GFP-PHDLA2 ΔBS	This paper	N/A
GFP-PHLDA2 PH	This paper	N/A
GFP-PHLDA2 ΔPH	This paper	N/A
RK5-Flag-GPAT3	This paper	N/A
Software and algorithms		
FlowJo v10	BD Biosciences	https://www.flowjo.com/
GraphPad Prism 8.0	GraphPad Software	https://www.graphpad.com/
CRISPOR	Concordet et al., 2018[74]	http://crispor.tefor.net/crispor.py
MAGeCK	Li et al., 2014[42]	https://github.com/liulab-dfci/MAGeCK
R (v 4.0.5)	R project	http://r-project.org/
Other		
Liu human CRISPR knockout library	Addgene	1000000132